# INFORMATION TO USERS

This manuscript has been reproduced from the microfilm master. UMI films the text directly from the original or copy submitted. Thus, some thesis and dissertation copies are in typewriter face, while others may be from any type of computer printer.

**The quality of this reproduction is dependent upon the quality of the copy submitted.** Broken or indistinct print, colored or poor quality illustrations and photographs, print bleedthrough, substandard margins, and improper alignment can adversely affect reproduction.

In the unlikely event that the author did not send UMI a complete manuscript and there are missing pages, these will be noted. Also, if unauthorized copyright material had to be removed, a note will indicate the deletion.

Oversize materials (e.g., maps, drawings, charts) are reproduced by sectioning the original, beginning at the upper left-hand corner and continuing from left to right in equal sections with small overlaps.

Photographs included in the original manuscript have been reproduced xerographically in this copy. Higher quality 6" x 9" black and white photographic prints are available for any photographs or illustrations appearing in this copy for an additional charge. Contact UMI directly to order.

Bell & Howell Information and Learning
300 North Zeeb Road, Ann Arbor, MI 48106-1346 USA
800-521-0600

University of Alberta

# Fast-Beam-Laser Lifetime Measurements for Energy Levels in Singly-Ionized Lutetium and Thulium

by

Michelle Marilyn McCurdy

A thesis submitted to the Faculty of Graduate Studies and Research in partial fulfillment

of the requirements for the degree of Master of Science

Department of Physics

Edmonton, Alberta

Fall 1999

**University of Alberta**

**Library Release Form**

Name of Author: Michelle Marilyn McCurdy

Title of Thesis: Fast-Beam-Laser Lifetime Measurements for Energy Levels in Singly Ionized Lutetium and Thulium

Degree: Master of Science

Year this Degree Granted: 1999



michelle mccurdy

Physics Department
University of Alberta
Edmonton, Alberta T6G 2J1

Date: August 26, 1999

**University of Alberta**

**Faculty of Graduate Studies and Research**

The undersigned certify that they have read, and recommend to the Faculty of Graduate Studies and research for acceptance, a thesis entitled **Fast-Beam-Laser Lifetime Measurements for Energy Levels in Singly-Ionized Lutetium and Thulium** submitted by Michelle Marilyn McCurdy in partial fulfillment of the requirements for the degree of Master of Science.

Dr. E. H. Pinnington

Dr. J. A. Kernahan

Dr. D.P. Hube

Dr. G. Horlick

Date: August 12th 1999

**Abstract**

The radiative lifetimes of four levels in singly ionized lutetium (Lu II) and sixteen levels in singly ionized thulium (Tm II) have been measured using the fast beam-laser technique. The results for the lutetium experiment are in generally fair agreement with the HFR+CP calculation by Quinet et al. Additionally, our results show further evidence of hyperfine structure effects in Lu II. The levels in Tm II were studied in order to resolve disagreement between Anderson et al's experimental results and Quinet et al's theoretical calculations. For fourteen of the the fifteen levels for which there was significant discrepancy between experiment and calculation, our work on Tm II supported the experimental results quoted by Anderson within the quoted errors. In the remaining case, our result is intermediate between the experimental value reported by Anderson et al and the theoretical value reported by Quinet et al.

# ACKNOWLEDGEMENTS

I would like to thank my supervisor, Dr. Eric H. Pinnington, for his guidance and support throughout the past two years, as well as financial support for the past two summers.

I would like to extend my thanks to Dr. Georg Rieger for his assistance and cooperation in the laboratory over the past two years.

I would like to thank Derek McCurdy for his support and understanding during the two years I spent in the Master's program.

Finally, I would like to thank the Department of Physics for financial support during the past two years.

# TABLE OF CONTENTS

# LIST OF TABLES

# LIST OF FIGURES

# CHAPTER I: INTRODUCTION

## 1.1 Introduction

In the study of astrophysics, particularly in the consideration of stars, knowledge of the abundance distribution is an essential factor. Abundance values (chemical composition) are essential when constructing a model atmosphere, or when comparing a star to the sun. Abundances also provide information about the origin and evolution of stars and stellar systems, as well as allowing a test of the theories of nucleosynthesis (i.e. how, where, and when the elements are formed).

Rare-earth elements are of particular interest in astrophysics, as they have been observed in many Ap stars [1] as well as Am stars [2] and in the solar spectrum [3, 4, 5]. However, many of these observed transitions appear as medium or weak lines which are strongly blended with other lines resulting from more abundant elements. In order to disentangle these blends, the transition probabilities must be precisely known. Both abundance values and transition probabilities are strongly dependent on precise lifetime measurements.

Singly-ionized lutetium (Lu II) was chosen for study mainly because of the scarcity of experimental radiative lifetimes in the literature. Until recently, the only values available were the Aarhus beam-foil data [6], although some very recent precision measurements have been done using laser-induced fluorescence of a slow atomic beam [4], as well as those based on a laser-produced plasma followed by pulsed laser excitation and time-resolved detection [7]. Since beam-foil excitation is non-selective and subject to cascading errors, we have performed experiments using laser-induced fluorescence of

a fast ion beam to provide some reliable cascade-free radiative lifetime measurements for Lu II.

The choice of singly-ionized thulium (Tm II) as an element of study resulted from poor agreement between experimental lifetimes measured by Anderson et al [8] and theoretical HFR calculations by Quinet et al [9]. Although the results from the two groups are generally in fair to good agreement, there are some levels for which significant deviation is seen. Consequently, the decision was made to measure lifetimes for some of the levels for which the two groups did not agree, in the hopes of resolving the discrepancy. Sixteen levels were chosen for study, generally with lifetimes of around 20 ns.

The astrophysics laboratory at the University of Alberta has now been closed down to make way for a new mass spectrometer laboratory. As my thesis project was the last to be performed on the equipment, it was important that the reliability of the apparatus for longer lifetimes be established convincingly. The reliability of the Edmonton beam-laser technique for lifetimes shorter than 20 ns has been well established in the past [10, 11] but there has always been a concern that longer lifetimes may be subject to systematic problems. Tests were therefore made for possible systematic effects using the Tm II transitions studied in this project.

This experimental work is part of a team effort involving Dr. E.H. Pinnington, Dr. Georg Rieger, and myself. My contribution to the lutetium and thulium projects has included participation in the running of the experiments, repairs to the equipment, data acquisition, data analysis, and the survey of literature.

In this thesis, I describe the Lu II and Tm II experiments, which were performed at the University of Alberta, in addition to some background and theoretical discussion in an attempt to place the experimental work into a relevant context. Chapter 2 gives an overview of how the experimental lifetime measurements fit into the larger picture of oscillator strength and elemental abundance determination, and the justification for doing these lifetime measurements. In Chapter 3, I outline some of the theoretical work closely connected to the experiment. In Chapter 4, I describe the general procedure and experimental apparatus used to make the precision lifetime measurements, while Chapter 5 deals with the specifics of the LuII and TmII experiments, along with a discussion of the results obtained.

# CHAPTER II: ASTROPHYSICAL APPLICATIONS

## 2.1 Introduction

Almost any study of a particular stellar atmosphere must begin with an initial assumption of the chemical composition. The construction of the model photosphere will depend on it. As well, a star's evolution can be traced by tracing changes in its chemical composition. Any star will hold information about the composition of the material from which it was made. This information can give clues about the star's formation.

The starting point on the path to determining the chemical composition of a particular star is to discover the elemental abundances of the elements making up the star. The lifetime measurements of the astrophysics group at the University of Alberta are an important part of this analysis. Experimental lifetimes, combined with experimental branching fractions, yield the oscillator strengths required for the abundance analysis. The oscillator strength, also known as the f-value, can be physically described as the effective number of classical electron simple harmonic oscillators that would absorb radiation of a given wavelength as strongly as the atom does.

## 2.2 Stellar Abundance Analysis

There are two main iterative methods used for obtaining elemental abundances in stars. The first, used if there is severe blending in the line spectrum, is called spectral synthesis. The line spectrum is calculated including all possible lines contributing to the opacity at the wavelength of the line of interest. This theoretical spectrum is then compared with the observed spectrum. Parameters (usually the abundances of all the contributors, with oscillator strengths staying fixed) are then varied to obtain agreement between theory and observation. When a match is made, the value of the abundance

parameter is combined with abundance results from other lines to get a mean value, which is taken to be the element's abundance for that star. Although acceptable for solar analysis, this slow and tedious method is not easily extended for use in stellar analysis because models of stellar atmospheres are only theoretical constructs, with larger uncertainties than for the sun. As well, observed stellar spectra are of lower resolution than solar spectra, so it is not feasible to integrate over the line profile.

In the second method, a model is assumed first, after which line intensities and continuous intensities are calculated by integrating over the line profile, giving equivalent widths $W_\omega$, as defined in Section 2.4 below. These $W_\omega$'s are then compared with observed equivalent widths and the abundance is adjusted to get agreement (fixed oscillator strengths, calculated from experimental lifetimes, and branching fractions). These calculations are complicated by the need to sum over contributions from different layers in the source, i.e., the calculations must use some form of stellar model, defining T (the temperature), particle density n, etc. as a function of depth. (The method through which an appropriate stellar model is obtained is described in section 2.3.) The following paragraphs outline how the integration over the line profile to obtain equivalent width is performed.

The energy produced in the central layers of a star is transferred from one layer to the other by radiation. The radiation emitted at an angle $\theta$ from a depth of $\tau_\lambda$ is given by

$$I_\lambda(\theta) = \int_0^\infty S_\lambda(\tau_\lambda) \exp\left[-\tau_\lambda \sec\theta\right] \sec\theta \, d\tau_\lambda \qquad (eq\ 2.1)$$

where $I_\lambda$ is the emerging intensity at the angle $\theta$ to the normal, $S_\lambda$ is the source function, $\tau_\lambda$ is the optical depth, and $d\tau_\lambda$ depends on the continuous and line opacities.

Equation (2.1) is integrated over the photospheric layers in which the lines are formed; so we need to know temperature and density as functions of the optical depth. These can be obtained from the stellar model, hence, continuum and line intensities can be computed.

The source function $S_\lambda$ reduces to the Planck function $B_\lambda$ when local thermodynamic equilibrium is satisfied (a valid assumption for the deep photospheric layers where weak and medium-strong lines are formed). The level populations can then be deduced using the Boltzmann and Saha laws.

The absorption coefficient at a given wavelength depends on line profile (equivalent width; see section 2.4 below), oscillator strengths, and the level populations. So if an f-value for a particular line is assumed for a given stellar model, the abundance of the element giving that line can be determined.

The profile of the line in question is determined by the line absorption intensity I, which in turn is dependent upon $N_i$, the population of the lower level (related to abundance); a function H determining the line profile shape; $\alpha(\lambda_o)$, the absorption coefficient; and $f_{ik}$, the oscillator strength. H and $\alpha$ are dependent on Doppler broadening, while H is also dependent on collision or damping broadening, as discussed in Section 2.4 below. The calculated value for the equivalent width can then be obtained.

2.3 Stellar Model

The analysis of a stellar atmosphere requires that a rough model of that atmosphere be assumed. This may be done in a preliminary way using experimental values by first applying a universal curve of growth, calculated by the interpolation formula on the following page [12]

$$R_\upsilon = \left( \frac{1}{\kappa_\upsilon H} + \frac{1}{R_c} \right)^{-1} \qquad (eq\ 2.2)$$

where H is the effective height, $\kappa_\nu$ is the absorption coefficient, and $R_\nu$ represents the depression in the line. This formula leads to the number NH of absorbing atoms above $1 cm^2$ of the stellar surface, using a measured $W_\lambda$ and known f-values and the damping constant $\gamma$. By comparing the NH's for various excitation energies and ionization stages for the element of study, T (temperature) and $P_e$ (electron pressure) can be obtained from the Boltzmann and Saha equations; the Saha equation is shown below in equation 2.3 [13]

$$\log \frac{P_i}{P_o} = -\log P_e + \frac{5}{2} \log T + \log \frac{2u_i}{u_o} - \theta \chi_{ion} - 0.48 \qquad (eq\ 2.3)$$

where $P_i$, $P_e$, and $P_o$ are the partial pressures for the ion, the electron and the neutral atom, $\chi_{ion}$ is the energy of the ground state of the ion, $u_i$ and $u_o$ are the partition functions of the ion and the neutral atom, and $\theta = 5040/T$. These values for T and $P_e$ allow extension from the number of atoms in particular energy levels to the total number of all particles; or, the abundance distribution. This abundance distribution (if we know the degree of ionization) leads from the electron pressure $P_e$ to the gas pressure $P_g$. As well, the gravitational acceleration g can be calculated from the equation of hydrostatic equilibrium. Finally, these values are used to estimate a reasonable effective temperature $T_{eff}$, a value for g, and a chemical composition for the model stellar atmosphere. After the model atmosphere has been obtained, the equivalent widths $W_\omega$ may be obtained by integrating over the line profile.

## 2.4 Equivalent Width

The strength of an absorption line is directly related to the chemical abundance of the absorber. In order to eliminate experimental inconsistency due to the fact that different experimenters may look at the same line with instruments of different resolution, we speak of line strengths in terms of their equivalent widths. The equivalent width of an absorption line is defined as the characteristic width a line would require (assuming black body behavior) to absorb the same amount of radiation as the actual line, shown graphically as covering the same area on the graph. (Figure 2.1)

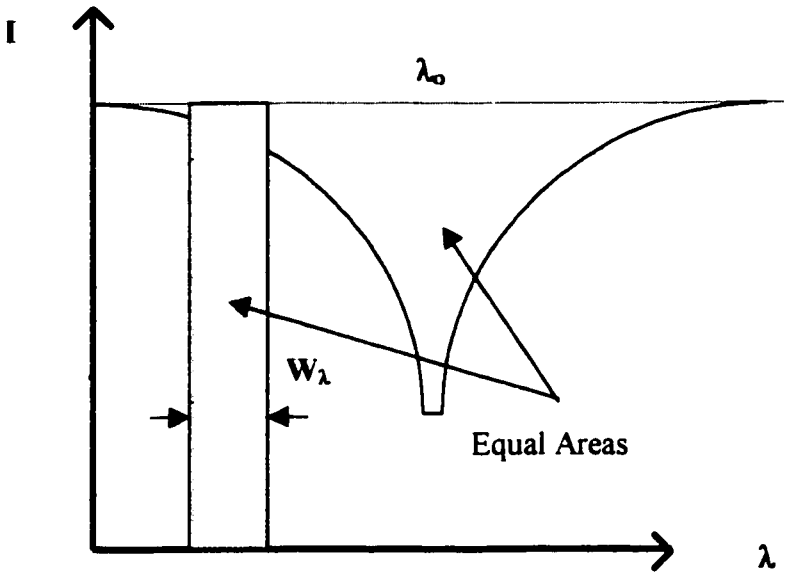


**Figure 2.1: Equivalent Width of an Absorption Line**

The equivalent width of an absorption line is described by the relation

$$W_\omega = \int \left(1 - \frac{I_\omega}{I_o}\right) d\omega \qquad (eq\ 2.4)$$

where $I_o$ is the intensity of radiation entering the gas (assuming a uniform plasma), and $I_\omega$ is the intensity of the radiation at frequency $\omega$ after passing through a thickness of the gas which is the solution to the equation of radiative transfer. The equation of radiative transfer is given by [14]

$$\frac{dI(\omega)}{dx} = \varepsilon(\omega) - \kappa(\omega) \cdot I(\omega) \qquad (eq.2.5)$$

and the solution is given by

$$I_\omega = I_o e^{-\tau} + \frac{\varepsilon_\omega}{\kappa_\omega}\left(1 - e^{-\tau}\right) \qquad (eq\ 2.6)$$

where $\tau$ is the transition's atomic lifetime, $\varepsilon_\omega$ is the emission coefficient, and $\kappa_\omega$ is the absorption coefficient of the gas.

In the calculation of equivalent width, two limiting cases arise, the optically thin and optically thick cases. In the optically thin case, (Figure 2.2) the absorption

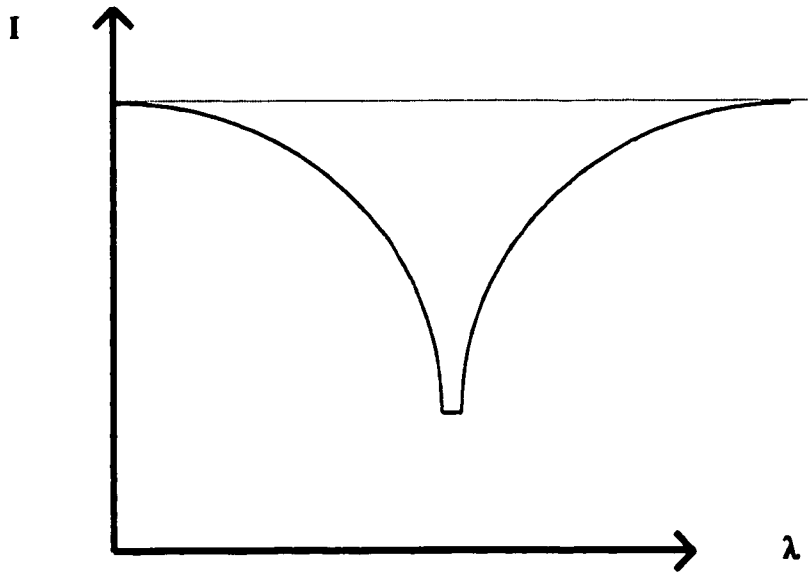


**Figure 2.2: Optically Thin Absorption Line**

of the plasma is not total, and the intensity never reaches zero. As a result, the equivalent width is directly proportional to the vapor density N, the column length L, and the oscillator strength f.

$$W_\omega = \frac{\pi e^2 fNL}{2\varepsilon_o mc} \qquad (eq\ 2.7)$$

In the optically thick case, however, the absorption is total, and the intensity reaches zero. (Figure 2.3) In this case, $W_\omega$ is no longer a simple linear function of N. An important

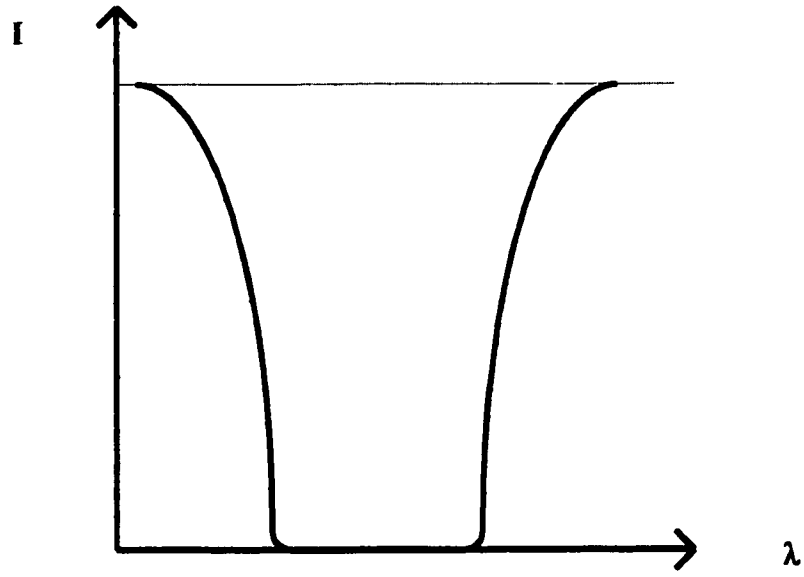


**Figure 2.3: Optically Thick Absorption Line**

factor in the equivalent width is the lineshape; as the wings of the line become important. Two main factors may contribute to the lineshape. The first factor is thermal broadening (Doppler broadening), which gives rise to a Gaussian intensity distribution

$$I = Ae^{-B(\Delta\lambda)^2} \qquad (eq\ 2.8)$$

which shows an exponential variation of intensity with wavelength. On the other hand, the second type of line shape arises as a result of damping broadening, due to the

collisions between atoms. This type of broadening will gave a Lorentzian intensity distribution

$$I = \frac{A'}{B'+(\Delta\lambda)^2} \qquad (eq\ 2.9)$$

which, in contrast to the Gaussian distribution, shows an inverse squared relation between intensity and wavelength. These different lineshapes lead to different equations for equivalent width. For the Doppler broadened optically thick line,

$$W_\omega = \Delta\sqrt{\ln\left(\frac{\sqrt{\pi}e^2 fNL}{\varepsilon_o mc\Delta}\right)} \qquad (eq\ 2.10)$$

where

$$\Delta = 2\left(\frac{\omega_o}{c}\right)\sqrt{\frac{2kT}{M}} \qquad (eq.\ 2.11)$$

For the damping broadened optically thick line,

$$W_\omega = \sqrt{\frac{e^2 fNL\Gamma}{\varepsilon_o mc}} \qquad (eq\ 2.12)$$

where $\Gamma$ is the natural width of the line, due to the fact that the line cannot have zero width; the Heisenberg uncertainty principle insists that it must have a width of at least

$$\Delta E = \frac{\hbar}{\Delta\tau} = \Gamma \qquad (eq\ 2.13)$$

Once the equivalent widths have been calculated, we can move on to the curve of growth.

## 2.5 The Curve of Growth

The equivalent width (intensity) of a spectral line varies as the number of atoms acting to produce it increases. The varying parameter is Nf (number of atoms x oscillator strength). Once the equivalent width has been obtained, it is plotted logarithmically

against the value Nf. The resulting graph is referred to as the curve of growth. As an example, an optically thin line, whose equivalent width is defined by eq 2.7, will be considered. Substituting the full expression for N and converting $W_\omega$ to $W_\lambda$, and then taking the logarithm, the relation becomes [13]

$$\log\frac{W_\lambda}{\lambda} = \log(NLf\lambda) - \frac{E_i}{2.303kT} + const \qquad (eq\ 2.14)$$

The graph of this relation reveals how equivalent width varies as a function of N, the number of atoms.

In general, as the quantity (NL) is increased for a given transition, the curve of growth contains three regions (see Figure 2.4 below). The optically thin region gives a

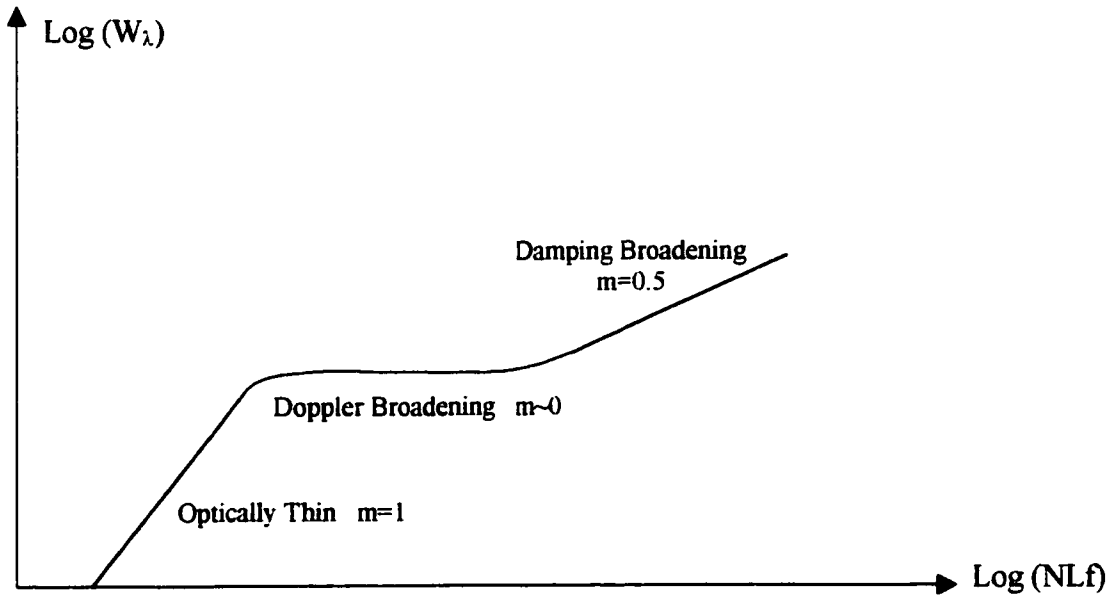


**Figure 2.4 A Sample Curve of Growth**

slope of unity. The center of the line becomes optically thick quickly and hence the Doppler profile is important, so the slope is almost zero. To still higher NL-values, the damping wings become important and the equivalent width increases again giving a slope

of 0.5. The most precise abundance measurements are made using lines on the optically thin part of the curve.

2.6 Experimental Branching Fractions

To obtain experimental branching fractions, we first start with the branching ratio for a particular line. This may be calculated as the ratio of the measured apparent line intensity to the relative quantum efficiency of the measurement device used. The branching ratio for any single line is then normalized to the dominant line from the upper level of the transition. Signal to noise weighting of each line leads to the weighted mean branching ratio. Finally, all the individual ratios are re-scaled in order that they add up to unity. These re-scaled ratios are known as the branching fractions. The branching fractions can then be combined with experimentally derived lifetimes to yield experimental oscillator strengths, which will likely be held as fixed parameters during stellar abundance analysis.

An atom in an excited state will decay spontaneously into a state of lower energy. This is not an instantaneous process; all atomic levels, with the exception of the ground state, decay with a finite lifetime $\tau$. This is typically measured experimentally and then combined with experimental branching fractions to obtain transition probabilities and hence oscillator strengths. It may also be obtained theoretically and then compared with experimentally determined results. The radiative lifetime and the branching fraction are related to the transition probabilities as follows:

$$\frac{1}{\tau_k} = \sum A_{ki} \qquad (eq\ 2.15)$$

$$B.F. = A_{ki} \cdot \tau_k \qquad (eq\ 2.16)$$

# CHAPTER III: ATOMIC STRUCTURE

## 3.1 Introduction

Since it is not practical to measure transition probabilities for all lines in a given spectrum, there will always be a need for a complete calculation. Furthermore, it is of fundamental importance to see how well current theoretical techniques can calculate atomic parameters.

The first thing necessary when dealing with the properties of a particular element is to establish its atomic structure. This structure must be calculated keeping in mind electronic correlations between valence electrons and between electrons and the ionic core. Since both are significant in the atomic structure of singly-ionized lutetium and thulium, these correlations must be represented in the Hamiltonian describing the atomic system.

The importance of dealing with both types of electron interactions (intravalence and core-valence) within the configuration interaction scheme causes many complexities. One way to address these difficulties is to follow the example of Migdalek and Baylis [15], where most of the intravalence correlation is represented in the configuration interaction. The core-valence interaction is then dealt with by adding a N-electron core polarization model potential $V_p$ to the Hamiltonian,

$$V_p(r) = \sum_{i=1}^{N} -\frac{\alpha_d r^2}{2\left(r^2 + r_c^2\right)^3} \qquad (eq\ 3.1)$$

where $\alpha_d$ is the static dipole polarizability of the core, and $r_c$ is arbitrarily chosen to approximate the size of the ionic core. Insertion of this term into the Hamiltonian requires a change of the dipole moment operator

$$\vec{d} = -\vec{r} \qquad (eq\ 3.2)$$

in the transition matrix element (for consistency) to

$$\vec{d} = -\vec{r} + \frac{\alpha_d \vec{r}}{\left(r^2 + r_c^2\right)^{\frac{3}{2}}} \qquad (eq\ 3.3)$$

The resulting modified Hamiltonian must be solved. The framework in which the polarization potentials mentioned above are used is the fully relativistic version of quantum mechanics based on the Dirac equation, known as the Dirac-Fock method. Since many configurations are considered at once, it is called the multi-configurational Dirca-Fock method (MCDF). A very different method is the pseudo-relativistic Hartree-Fock (HFR) method adapted from Cowan [16].

3.2 Relativistic Hartree-Fock

The first step in the HFR approach is to assume that a combination of N orthogonal one-electron orbitals may be used to approximate the wavefunction of the actual N-electron atomic system. Then the Schrodinger time-independent equation may be solved using the Hamiltonian

$$\mathrm{H} = \sum_{i}^{N}\left(\frac{p_i^2}{2m} - \frac{Ze^2}{r_i}\right) + \sum_{i>j}^{N}\frac{e^2}{r_{ij}} \qquad (eq\ 3.4)$$

The ground state of this atomic system is approximated as

$$\Psi(1,2,\ldots N) = \frac{1}{\sqrt{N}}\det\left\{\phi_1(1)\phi_2(2)\ldots\phi_N(N)\right\} \qquad (eq\ 3.5)$$

a Slater determinant which accounts for the Pauli exclusion principle, where the $\phi_N$'s refer to one-electron orbitals. The variational principle requires additionally that

$$\delta\langle\Psi|\mathrm{H}|\Psi\rangle = 0 \qquad (eq\ 3.6)$$

Once the Hamiltonian and the ground state wavefunction have been approximated, the next step is to solve the equation

$$H\Psi = E_{av}\Psi \qquad (eq\ 3.7)$$

Since these calculations are not performed at the University of Alberta, they will only be briefly outlined.

In order to account for the effects of relativity in the calculations, the Hamiltonian may be modified. Three new terms are added to the Hamiltonian in the form of a perturbation. The first term, called the mass-velocity term, arises from the relativistic variation of mass with velocity. The second term is known as the Darwin term, and is due to the relativistic non-localizability of the electron. The third relativistic term, the spin-orbit term, represents the magnetic interaction energy between the electron's spin magnetic moment and the magnetic field seen by the electron as a result of its orbital motion through the nucleus' electric field. These three terms may be used to modify the non-relativistic Hamiltonian to include relativistic effects. [16]

There is not a direct method of solving the Hartree-Fock equations, as they are coupled, nonlinear, and integrodifferential. Solving of any Hartree-Fock equations requires knowledge of all the other orbitals. Therefore, a self-consistent approach is used to obtain these orbitals, where initial orbitals are selected more or less arbitrarily. These assumed spin orbitals allow calculations of the Coulomb and spin integrals, and improved orbitals may be calculated using the Hartree-Fock equation. The calculations are repeated iteratively until successive cycles yield good agreements between the orbitals.

Once the orbitals are known, the energy levels can be calculated. The radial parameters are then adjusted by an iterative procedure to give the best least-squares fit

between the calculated and observed level energies. The variational parameters include $E_{av}$, the center of gravity energies; $F^k$ and $G^k$, respectively the direct and exchange interaction terms; the spin-orbit integrals $\xi$, and some configuration interaction integrals $R^k$ related to experimentally examined configurations. The end result is a set of fitted energy levels $E_N$ which compose the atomic structure of the ion in question, and the energy eigenfunctions $\Psi_N$, composed of a linear combination of the one-electron orbitals $\phi_N$ calculated earlier. These are related by:

$$E_i \Psi_i = E_i \left( a\phi_{HFR1} + b\phi_{HFR2} + \ldots \right) \qquad (eq\ 3.8)$$

in which a , b, ..., n represent the percentages of each of the HFR one-electron orbitals in the wavefunction $\Psi_N$ satisfying the eigenvalue equation.

Knowing the level energies and the eigenvectors (combination wavefunctions) with which they are associated, theoretical values for the atomic lifetimes ($\tau_{HFR}$) and branching fractions ($b.f._{HFR}$) may be calculated. The HFR lifetimes and branching fractions then are used to find theoretical oscillator strengths ($f_{HFR}$).

3.3 The HFR+CP Technique

The calculation technique employed by the Liege group, whose results are compared in Chapter 5 with our experimental values for the lifetimes of the 16 levels in Tm II and 4 levels in Lu II, is actually a combination of the core-polarization methods of Migdalek and Baylis, and of Cowan's pseudo-relativistic Hartree-Fock method, as described in the previous two sections. By means of the simple non-relativistic Cowan method, the initial radial wavefunctions are varied to minimize the configuration energy (as in eq 3.6 above). To account for the major relativistic effects, the mass-velocity, Darwin and spin-orbit terms mentioned in Section 3.2 above are added to the non-

relativistic Hamiltonian as a perturbation. The perturbed Hamiltonian is additionally modified to contain the core-polarization term and the modified dipole moment operator described in equations 3.1 and 3.2. The calculation then proceeds as was outlined in Section 3.2.

3.4 Hyperfine Splitting in Singly Ionized Lutetium

One important atomic feature of singly ionized lutetium, which affected the experimental lifetime measurements, is its large hyperfine structures. The magnetic interaction between the nucleus and an electron splits an atomic term specified by $\vec{J}$ into a number of hyperfine levels, characterized by the value of $\vec{F}$. $\vec{F}$ is defined as the vector sum (see Figure 3.1 showing the vector addition) of the total electron angular momentum

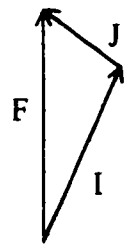


**Fig 3.1 The Vector Model Representing** $\vec{I} + \vec{J} = \vec{F}$

$\vec{J}$ and the angular momentum of the nucleus, $\vec{I}$. The splitting due to the magnetic dipole interaction is calculated via the following:

$$\Delta E_{MD} = \frac{A}{2}\{F(F+1) - I(I+1) - J(J+1)\} \qquad (eq.\ 3.9)$$

In the case of singly-ionized lutetium we must also include the electric quadrupole hyperfine structure effects. These result because the nucleus possesses electromagnetic multipole moments which interact with the electromagnetic field produced at the nucleus

by the electrons. The electric quadrupole moment is caused by the departure from a spherical charge distribution in the nucleus. The energy shift due to the electric quadrupole interaction is given by

$$\Delta E_{EQ} = \frac{B}{4}\left\{\frac{\frac{3}{2}\left[F(F+1)-I(I+1)-J(J+1)\right]-2I(I+1)J(J+1)}{I(2I-1)(2J-1)}\right\} \qquad (eq\ 3.10)$$

Two levels of interest in our experiment were pumped from the triplet D term in LuII, $^3D_3$. This level gives rise to the hyperfine structure calculated below. The energy shift due to hyperfine splitting, combining the magnetic dipole and electric quadrupole shifts, is given by the following:

$$\Delta E_{HYPERFINE} = \Delta E_{M\ DIPOLE} + \Delta E_{E\ QUADRUPOLE} \qquad (eq\ 3.11)$$

where the dipole and quadrupole terms are given by equations 3.9 and 3.10, respectively.

For the triplet D level, the total electron angular momentum J is equal to 3, and the angular momentum of the nucleus I is equal to 7/2 [17]. The total angular momentum F can assume values from 1/ 2 to 13/2. The A and B values to be used in equations 3.9 and 3.10 are obtained from the paper by Steudel [18]. Figure 3.2 below, shows the individual terms resulting from the magnetic dipole and electric quadrupole contributions to the hyperfine structure of Lu II.

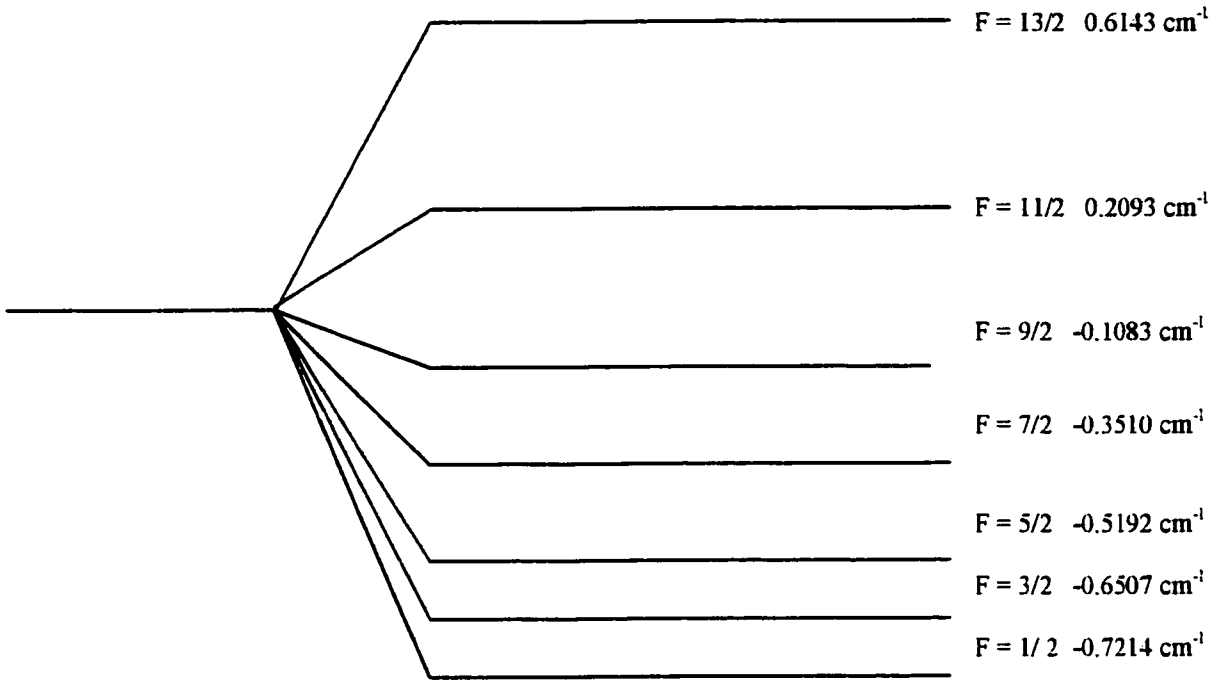


**Figure 3.2 The Hyperfine Splitting of the $^3D_3$ Term in Lu II**

These splitting terms should give rise to a line with an observed width of 1.33 $cm^{-1}$, which will mean a wavelength spread of 0.011 nm for the lines at 289.6 nm and 291.2 nm.

A wavelength spread is also expected due to hyperfine effects for the line pumped from the $^3D_2$ level. Using the A and B values from Steudel, and equation 3.11, the energy spread is expected to be 1.043 $cm^{-1}$, which corresponds to a wavelength spread of 0.0099 nm, as the line appears at 307.8 nm.

The hyperfine structure for the $^1D_2 - {}^1F_3$ transition at 279.7 nm is expected to be very small, provided the $^1D_2$ level is purely a singlet. A significant width for this resonance would suggest a mixture of pure states, and the level may contain a triplet component.

# CHAPTER IV: EXPERIMENTAL SETUP

## 4.1 Introduction

The method employed by the astrophysics group at the University of Alberta to measure atomic lifetimes is known as the fast-beam-laser method. In this method, a laser beam of certain specified wavelength is crossed with a fast ion beam to excite energy levels of interest in that particular ion. A fast ion beam is used because a high beam velocity will give better time resolution, which is very important when measuring short lifetimes (i.e. lifetimes shorter than about 20 ns).

Formerly, a technique known as the beam-foil method was used, whereby an ion beam passes through a thin carbon foil and becomes excited in that manner [19]. One major problem with the beam-foil method is the non-selective nature of the excitation process. Many levels will be populated at the same time. The electrons cascade down through several levels before reaching the level of interest, resulting in the superposition of several exponential terms in the recorded decay curve. Because of the statistical fluctuations in the signal, it is difficult to separate these exponential components in the data analysis. Consequently it is not possible to guarantee that the final measured lifetime is not subject to significant systematic errors. This problem is easily solved for our purposes by switching to the beam-laser method.

In the beam-laser experiment the laser wavelength is tuned to the same value as the wavelength of the transition in question (usually between an excited level and a ground or metastable state). That way, the only level populated will be the one with the selected energy difference. The decay curve will then involve just one exponential

representing the transition between the two levels, provided there are not other decay routes available to the level with non-zero transition probability. [20]

4.2 Apparatus

The experimental setup consists of three major components: the accelerator/ion source, the data collection system, and the laser setup. A schematic of the system is shown in Figure 4.1 on the following page.

4.2.1 *Accelerator/Ion Source*

The ion source produces the ions of interest. It consists of a Danfysik 911a hollow cathode ion source, including a tungsten filament for heating, an aperture for focusing, and an oven to deliver the source element. A small hollow crucible is mounted on the end of the oven, and this crucible is filled with the element of interest.

To produce an ion beam, the element must be heated to its vaporization temperature. First, the system is pumped out to approximately 2-3 x $10^{-6}$ torr. The tungsten filament is then slowly heated, with the oven located far from its position. At the same time, the 250V anode voltage is applied. When the filament is heated by a current of up to 25 amps, argon gas is slowly admitted into the system in order to obtain a discharge of the anode voltage. Once this discharge is obtained and a steady anode current is produced, thermal energy is produced in the source. In addition, the oven may be moved back and forth within the source in order to vary the temperature of the element. As the oven is moved closer to the filament and discharge, the temperature of the element inside rises, until its vaporization temperature is reached. The positive ions produced are then accelerated through a potential difference, which may be varied between -150kV to -350kV.

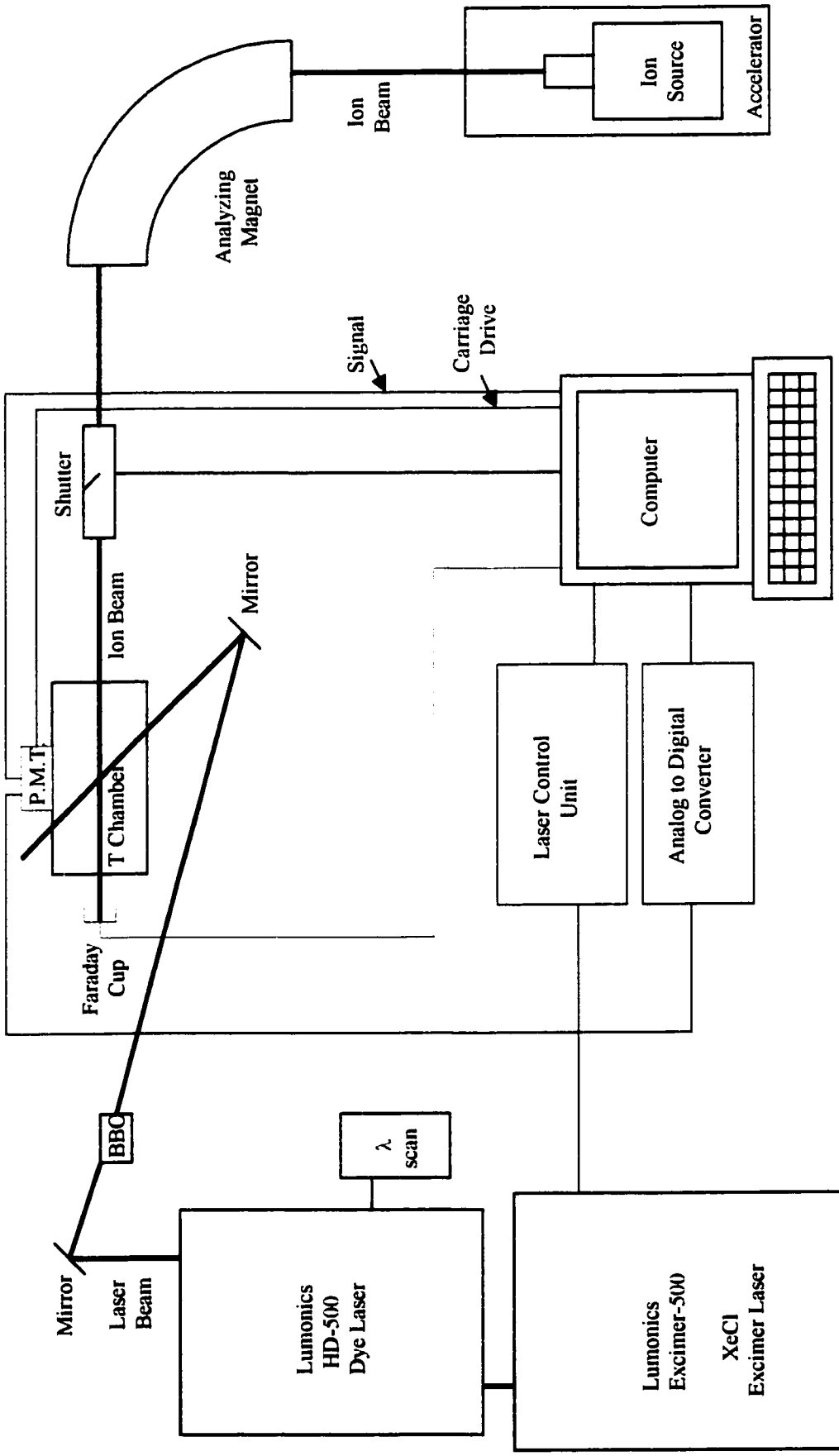


**Figure 4.1: The beam-laser experimental arrangement**

There are various electrostatic lenses available to shape and focus the ion beam; an extraction lens, a triplet lens, and a parallel lens. In practice, the parallel lens has little effect and so is seldom used. The ion beam is defined by the 5mm entrance to the target chamber as well as the 8mm diameter of the Faraday cup (where the beam current is measured and relayed to the computer).

Although the crucible is filled with the element of study in essentially pure form, there may be other components in the ion beam, most notably the argon gas used for the discharge. To isolate the element, the beam is passed through a mass-analyzing magnet. The magnet bends the components of the beam according to atomic mass, so that only the ions with the selected atomic mass will be focused into the target chamber. However, this technique is not perfect, and trouble arises when the source is contaminated by an element of mass similar to the element of study. (This will be discussed in detail in Chapter 5.) The amount of beam current, as measured by a shielded Faraday cup located just beyond the target chamber, can then be controlled by varying the proximity of the oven to the filament and discharge. There is also some additional heat provided by the magnet in the source, whose main purpose it is to counterbalance the effects of the magnetic field produced by the current flowing in the filament coils. At first, the beam current is quite small as there are only a few ions excited. However, as the temperature is increased towards the vaporization point, the beam current increases to a maximum value. The beam current is stabilized at a maximum value by optimization of the electrostatic lenses, the source magnet, and the analyzing magnet. The beam is then directed into the target chamber.

4.2.2 *The Lasers*

For this type of experiment it is essential to be able to tune the laser wavelength precisely. The laser setup normally consists of a Lumonics HD-500 dye laser pumped by a Lumonics Excimer-500 XeCl excimer laser. The operation of the two lasers is briefly described in the following paragraphs.

An excimer is a molecule which is only stable in an excited state, hence it effectively has no lower level. Formation of this excimer molecule will result in a population inversion, as the lower (ground) state will be empty. This excimer formation is accomplished in our XeCl excimer through excitation of the xenon by an electrical discharge. The excited xenon ions will then combine with the chlorine atoms from the HCl gas which is admitted into the system, forming the XeCl excimer molecule. An ultraviolet spark trigger will give rise to pulsed laser radiation, after which the XeCl molecule dissociates and the process repeats at an interval decided by the laser control unit. Our excimer laser provides pulsed laser light at a wavelength of 308 nm.

Our dye laser operates on the principle that many organic compounds which absorb strongly in the visible and near ultraviolet regions of the spectrum also fluoresce; providing radiation covering a large wavelength range. Each energy level in the molecule also has associated with it an array of vibrational and rotational levels. The vibrational levels are spaced at intervals of order $10^3$ $cm^{-1}$, while the rotational level spacings are of order 10 $cm^{-1}$. Due to high density in the liquid dye, the frequently occurring collisions among the energy levels smear out these rotational and vibrational levels to form continuous energy bands. When the dye is illuminated by light with wavelength falling within the absorption band, molecules are optically excited from the

ground state into some rotational or vibrational singlet level. Then collisions dissipate excess vibrational energy of that singlet state, on a time scale of picoseconds. From there, the molecules may decay by spontaneous emission into any of the rotational or vibrational levels of the ground state, after which non-radiative relaxation will return the molecule to the lowest level of the ground state (Figure 4.2). Pumping radiation (in our case from the excimer laser) gives rise to a 'population inversion', since there are no molecules in the upper levels of the ground state, after which laser action is possible. In our dye laser, the organic

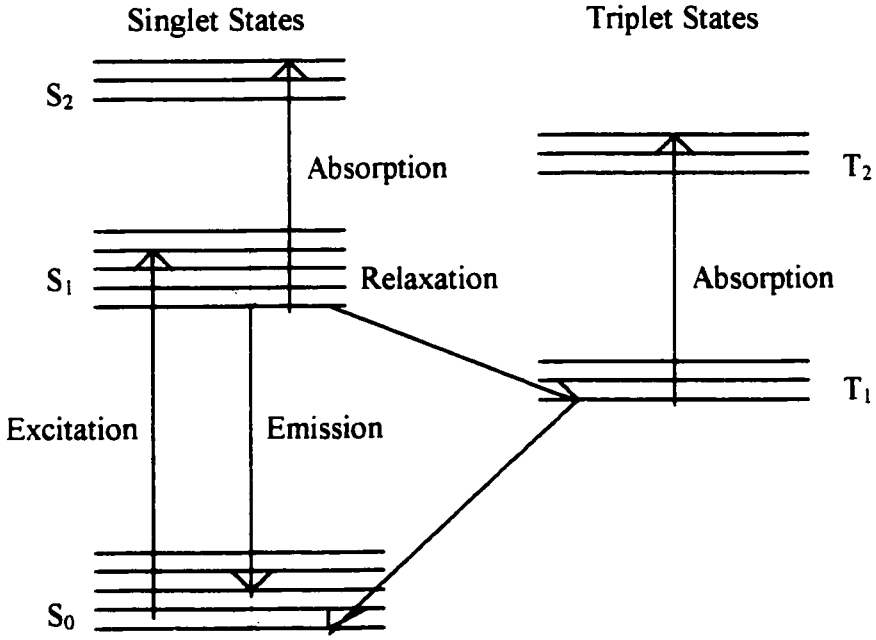


**Figure 4.2: Schematic Energy Level Diagram of a Dye Molecule (after Corney [21])**

dye molecules are dissolved in a solvent and circulated through the laser. The excimer laser output is directed into the laser chamber, where it crosses with the dye cell and excites the dye molecules. A diffraction grating at the end of the dye laser cavity is used to tune to the desired wavelength, giving output radiation which is coherent and tunable

over the continuous energy band of the selected dye molecules. The available dyes allow wavelengths of approximately 330-600 nm.

Since the majority of transitions interesting to us lie below 330 nm, the laser output is commonly passed through a BBO frequency-doubling crystal, in which the first harmonic of the incident radiation is produced, thus giving half the incident wavelength. Various lenses, mirrors and prisms shape and direct the beam before it is sent into the target chamber at a 45° angle to the ion beam, as shown in Figure 4.3.

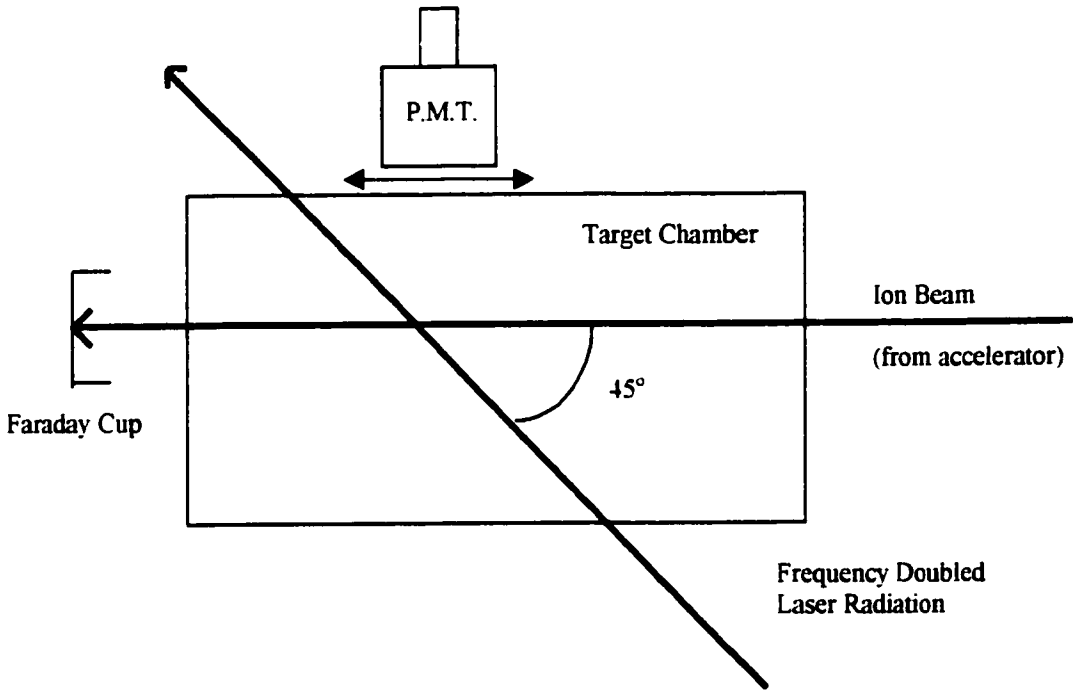


**Figure 4. 3: 45° Excitation of a Fast Ion Beam**

*4.2.3 Data Collection System*

When the laser beam crosses the ion beam, energy levels are excited. These excited levels will decay spontaneously by fluorescence, whereby light is emitted at wavelengths characteristic of the transitions. This light is picked up by the optical detection system. As the fluorescing ions move downstream along the ion beam, away

from the region of the excitation, the intensity of the fluorescence will drop off as a function of the ion's distance from the excitation. Measuring the intensity as a function of distance will give a relation yielding the lifetime of the excited level, and allows a time-dependent process to be measured as a distance-dependent one.

The fluorescence is detected by a photomultiplier, chosen because of its region of sensitivity. For example, a Hamamatsu 431 Solar Blind photomultiplier is often used because of its insensitivity outside the region of 160-320 nm. This greatly reduces the background contribution due to excitation of residual gas molecules which tend to radiate in the visible and infrared regions (above 320 nm), while remaining sensitive in the region of the transitions [22]. When the transitions are of wavelength longer than 320 nm, it becomes necessary to use an EMI 9789B photomultiplier. The photomultiplier is mounted on a track on top of the target chamber, as seen in Figure 4.4, and is aligned

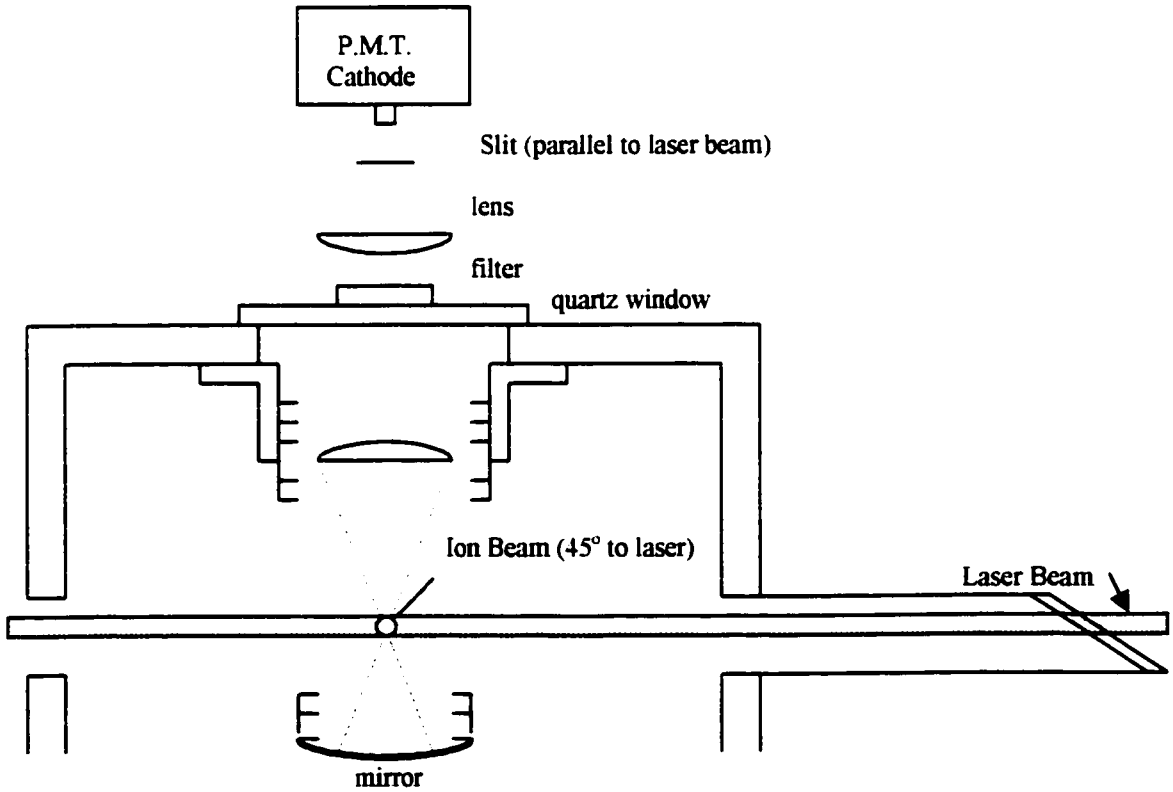


**Figure 4.4: Photomultiplier and target chamber**

with an observation window on the chamber. There is an electronically controlled stepping motor connected to the track, which advances the photomultiplier assembly in pre-determined steps (typically 0.25 mm for the lutetium experiment, 0.25-1.2 mm for the thulium experiment), starting at or near the point of excitation and moving downstream along the direction of the ion beam as the decay occurs.

For the first half of a decay curve measurement, the photomultiplier is moved parallel to the ion beam. The photomultiplier is operated in charge-integration mode, to avoid errors due to charge pile-up, which occur in single-photon counting. The intensity of the fluorescence is integrated for two seconds at every 'step' (size determined by the computer's setting of the stepping motor) for a preset number of data points (typically 40). Then, the photomultiplier is moved back in the direction anti-parallel to the ion beam. This is intended to average out any errors which might be caused by variation in the laser power or ion beam current, as the two halves of the decay curve will later be folded over on top of one another and summed. The interface between the optical detection system and the computer consists of a laser control unit, a TN 1211-A analog-to-digital converter (ADC), and an Ortec 974 Quad Counter/timer. The laser control unit generates trigger pulses to control the laser repetition rate, gating pulses to prompt data measurement, and a switch signal to identify a gating pulse as either A or B. The ADC receives a gating pulse which prompts it to measure the counts in coincidence with the gating pulse, and also converts this coincidence signal to a digital output. This digital signal is then sent to the Ortec 974 counter which has been told by the laser control unit into which channel (A, B, A', or B') to record it.

The computer is set up to receive the data from the Ortec 974 counter via the program developed at the University of Alberta. As well, the computer controls a beam shutter, opening or closing it every 2 seconds. The stepping motor apparatus, which moves the photomultiplier incrementally, is also controlled by the computer through an electronic interface. Further details are given in section 4.5 below.

4.3 Preparation

The first thing which must be done, before a decay curve can be measured but after an ion beam has been obtained, is to obtain a resonance; that is, to find the laser wavelength for which maximum excitation takes place. The effective wavelength (which must be corrected for Doppler shift and wavelength in air) must be precisely related to the wavelength characterizing the transition in question. First, calibration of the dye laser must take place, by means of a neon or krypton lamp. The spectrum from the reference lamp is displayed on an oscilloscope, using a Spex ¾-metre spectrometer fitted with a Reticon RL0512SAQ silicon photodiode detector. A description of the operation and characteristics of a silicon photodiode array detector can be found in the paper by Horlick [23]. The roughly calibrated laser light is then also shone into the Spex, and is displayed accordingly on the scope. The wavelength difference between the calibration line and the laser line appears on the scope as a time difference in the horizontal sweep. This is converted to Angstroms by means of a dispersion chart calibrated for the Spex. In this way the laser wavelength can be routinely measured to an accuracy of approximately 0.01 nm. This calibration must be performed whenever a significantly different wavelength region is desired, to ensure the calibration remains valid.

Next, the properly calibrated dye laser is set to the wavelength corresponding to the transition, corrected for Doppler shift, the wavelength in air, the effect of the frequency-doubling crystal, and the order ($1^{st}$, $2^{nd}$, or $3^{rd}$) of the transition. A spectrum is then measured, and displayed on the computer screen. For a spectrum, the detection optics do not move along the ion beam. Rather, the photomultiplier is placed at the position of maximum signal intensity and the wavelength of the dye laser is varied over a short range by means of a laser stepping motor, in steps of either 0.0005, 0.0010, or 0.0020 nm, depending on the width of the resonance. The fluorescence at each step is displayed on the computer screen (Figure 4.5). When a maximum in intensity is reached,

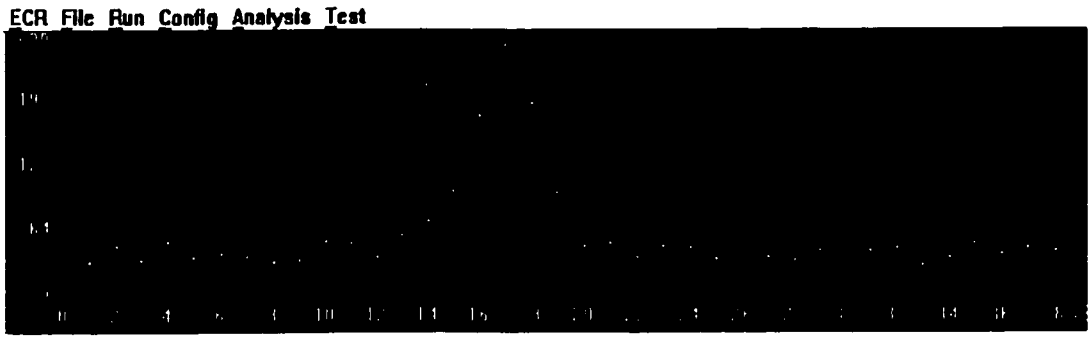


**Figure 4.5: Computer Screen Display of a Typical Spectrum (Yb II, 218.6 nm)**

thus signifying a resonance, the dye laser is set to that wavelength in preparation for the decay curve measurement.

4.4 Beam Velocity

The beam velocity requires careful measurement as it figures directly into the lifetime calculation. The high velocity of the ion beam and the fact that the two beams cross at a 45° angle give rise to a Doppler shift between the observed wavelength of the transition and its actual wavelength. This shift is used to measure the beam velocity.

The laser is arranged so that after it crosses the ion beam (at 45°) it is then reflected back along the same path to cross the ion beam again. The ion bean is excited on each crossing. The excitation from the first crossing will show a difference between the actual (wavelength of the transition in stationary atoms) and observed values of:

$$\Delta\lambda = -\lambda\frac{v}{c}\cos 45^{o} \qquad (eq\ 4.4.1)$$

The excitation from the reflected laser beam will give a difference of

$$\Delta\lambda = \lambda\frac{v}{c}\cos 45^{o} \qquad (eq\ 4.4.2)$$

Measurement of $\Delta\lambda$ will thus allow calculation of v. However, it is difficult to measure $\Delta\lambda$ directly. Since the calibration lines are generally quite far apart and the laser scanning mechanism is not perfectly linear, two calibration lines are chosen with a wavelength difference of approximately twice the Doppler shift. The one with the greater wavelength will be excited on the first passage (and hence will have an observed wavelength lower than actual) and the lower wavelength resonance will be excited on the second, and conversely will have its observed wavelength higher than actual. This effect will bring the two observed resonances close together, and the wavelength difference $\Delta\lambda_L$ is easily measured. The difference between the actual resonant wavelengths $\Delta\lambda_o$ is calculated from tabulated values. The average $\Delta\lambda$ between the actual and observed transitions is

$$\Delta\lambda = \frac{(\Delta\lambda_o - \Delta\lambda_L)}{2} \qquad (eq\ 4.4.3)$$

$\Delta\lambda$ can then be substituted into equation 4.4.1 or 4.4.2 to obtain v. This method of velocity determination has a precision of about 0.5%. [24]

4.5 Decay Curve Measurement

A decay curve is obtained by recording the intensity of the fluorescence of an ion as it moves along the beam as a function of its distance downstream. As mentioned in section 4.2.3, the first half of the measurement is taken in the direction parallel to the ion beam, and the second half is taken anti-parallel. The first half typically consists of 40-45 data points made as the detection system is moved incrementally along the ion beam, and the second half is the same number of points taken on the return trip. One of these 80-90 point round trips is called a sweep. Ideally between 5-10 successive sweeps are added together to yield a single decay curve.

The background contributions are measured along with the total signal, so the background signal can be accounted for when calculating the net signal. This background comes primarily from two sources; the laser scattered light produced by the laser beams going through the windows and also hitting the residual gas in the target chamber; and the excitation of the ion beam by the chamber's residual gas. Although the target chamber pressure is maintained at a low level (typically $2 \cdot 10^{-7}$ torr) and the solar blind multiplier is not sensitive in the visible region, the scattered light is not negligible and must be considered. For each data point, the total signal T (A gate), the laser scattered light L (A' gate), and the beam background B (B gate) are measured, as well as the total integrated beam current I. The gating electronics generate a timing sequence to open and close the beam shutter and take the appropriate measurements as follows.

With the beam shutter open (i.e., ion beam on) the laser is triggered by the laser control unit (LCU) to generate a pulse. This pulse prepares the computer to read the analog-to-digital (ADC) signal and to store the measurement. This process lasts 1 μs.

Next, an "A" gating pulse 3 μs wide activates the ADC to begin recording the total signal T. These gating pulses come every 10 ms when the laser repetition rate is 100 Hz. Approximately 5 ms after this "A" gate, the laser control unit generates a switch signal which designates the next 3 μs gating pulse as a "B" gate. The B gate measures the beam background (B), since presumably the excited level has completely decayed after 5 ms has passed and the only signal left is due to beam background. These A and B gates repeat 200 times each during the 2 seconds the beam shutter remains open, summing for a running total. For the second half of the measurement, the beam shutter is closed (i.e. ion beam is off, only the laser is in the target chamber) and the A and B counters are reset to zero. The A gate now measures the laser background (L).

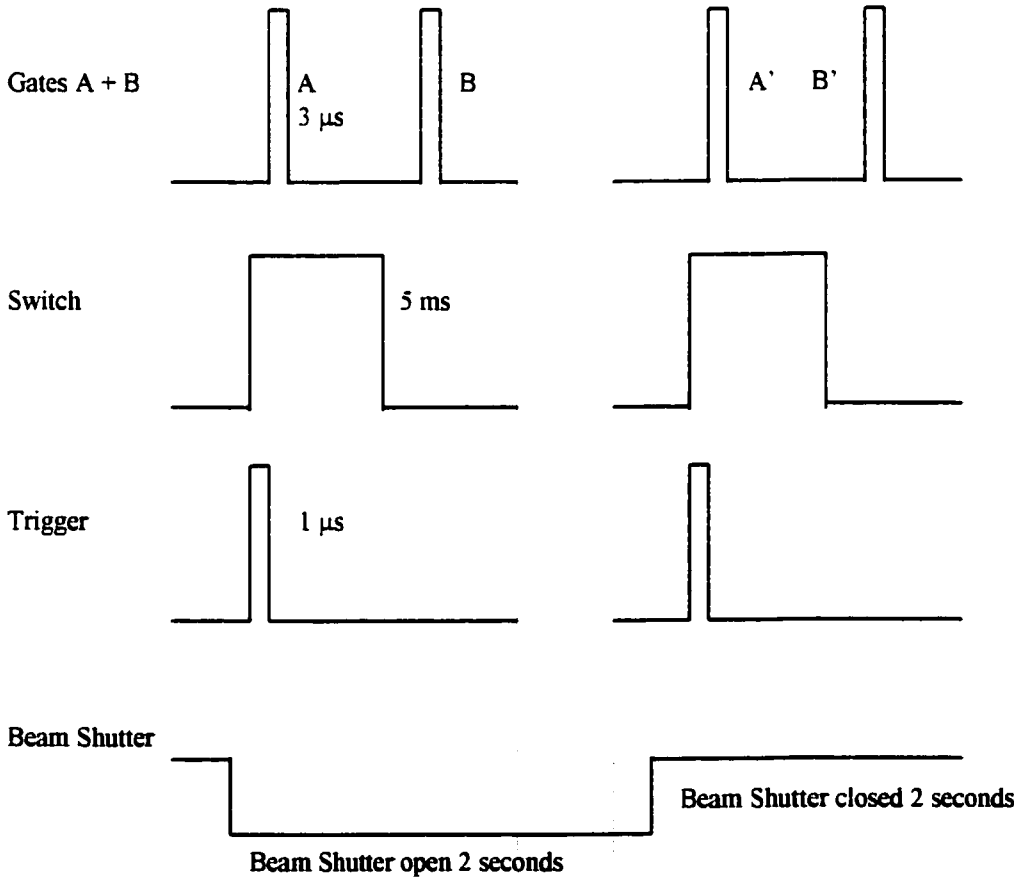


**Figure 4.6: Timing Sequence for Data Collection Unit**

For each data point the ion beam current (I) is also measured by a shielded Faraday cup positioned beyond the target chamber. The net signal for each point is then T-L-B, while that point will be normalized to the beam current I and weighted in the fit routine as (T+L+B), assuming Poisson statistics.

In all, seven measurements are displayed on the computer screen: 1) the position of the photomultiplier in mm x 100, 2) the total signal T, 3) the ion beam background B, 4) the ion beam current I, 5) the laser power (not connected), 6) the laser scattered light L, and finally 7) the net signal T-L-B. A typical data set is shown in Figure 4.7.

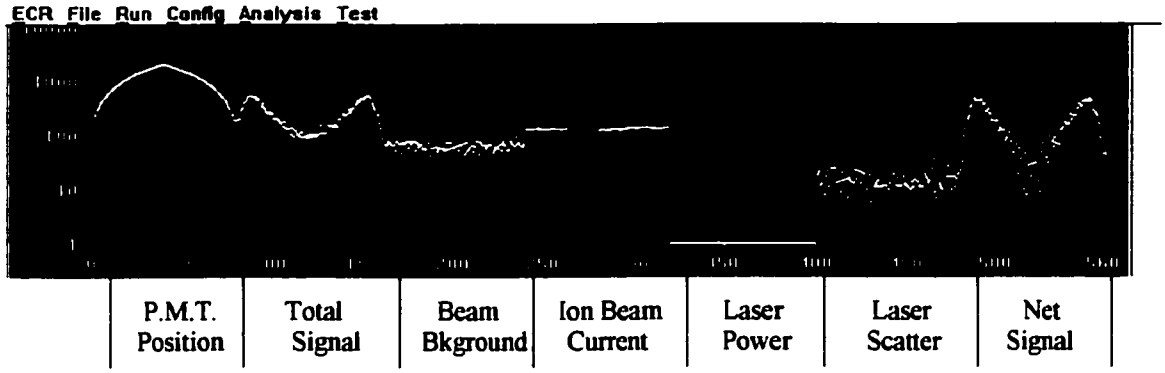


**Figure 4.7: Typical Data Set**

4.6 Fitting the Decay Curve

Once a decay curve is obtained, the lifetime ($\tau$) can be derived. For the lutetium and thulium experiments, the energy levels of interest were populated from lower metastable states, rather than the ground state. As a result, the populations were such that a good decay curve would only be obtained if data collection were begun near the excitation region. A difficulty arising from this was the fact that the lifetimes were often expected to be relatively short, of the order of 4 ns. At an acceleration voltage of 300kv (which was the energy used for the shorter lifetimes) this time period corresponds to a distance of just 2.5 mm. So, in order to get good photon statistics, the excitation region is

included in the decay curve. The measurement is started before the excitation region, on the upstream side of the excitation. Although the intensity of the fluorescence normally follows a simple exponential decay with distance, this is not the case in the excitation region. Therefore, a specialized fitting routine taking into account the shape of the observation window must be used. Independent measurements have shown the observation window of our optical system to be approximately Gaussian with a FWHM (full width at half-maximum) of about 2.5 mm. [25] The fitting program used to fit the data to a combination of a Gaussian and an exponential is called GFIT.

Some initial estimates are required for the program GFIT, including values for the level lifetime and the size of the observation region. The program then attempts to fit the data points to a combination of an exponential and a Gaussian. The process may be repeated, with modified initial parameters and with the ability to truncate points from the beginning or end of the curve, until a suitable fit is obtained. The lifetime may then be read from the output of the program, along with the other parameters.

# CHAPTER V: THE LUTETIUM AND THULIUM EXPERIMENTS

## 5.1 Introduction

The elements lutetium and thulium, of the lanthanide group, are of particular astrophysical interest in the study of certain chemically peculiar and rapidly oscillating Ap stars, as well as in determination of solar abundances, as described in section 2.2. As a result, it is desired to have as comprehensive a set of lifetime measurements for these elements as possible.

Very few experimental values have been published for the radiative lifetimes of singly ionized lutetium (Lu II), those few being limited to the Aarhus beam-foil data [6], and, more recently, measurements using laser-induced fluorescence of a slow atomic beam [4] and measurements based on a laser-produced plasma followed by pulsed laser excitation and time resolved detection [7]. In order to extend this data bank, lifetimes for four energy levels of the 5d6p configuration of LuII were measured using the fast beam laser-induced fluorescence method, with the intent to provide precision cascade-free lifetime measurements for those levels.

In contrast, a comprehensive set of lifetime measurements has recently been published for transitions in neutral and singly-ionized thulium [8]. In addition, theoretical lifetimes of TmII levels calculated using the relativistic Hartree-Fock method have been published [9]. For the most part, there is fair to good agreement between the theoretical and experimental lifetime values. However, for a number levels there is significant deviation. As a result, we have measured fifteen of the Tm II lines for which experiment and theory disagree, plus one additional level selected to give a consistency check. The levels were chosen for the fact that most have lifetimes around 20 ns, with a

few longer than 20 ns. As a result, the levels provide a test of our approach for those lifetimes, as well as attempting to confirm or disprove the contradicting experimental and theoretical values.

5.2 The Lutetium Experiment

The Lu II 5d6p levels studied were populated from the metastable 5d6s levels, using frequency-doubled radiation from the excimer pumped Lumonics HD-500 dye laser. Other Lu II levels were not examined either because they were too high in energy to be excited by our available set-up, or because the transitions were too weak to obtain sufficient signal to noise ratio.

Several problems were encountered during the lutetium experiment. Firstly, the only LS-coupling allowed ground state transition above 200 nm is to the 6s6p $^1P_0$ term; however the lifetime of this transition was too short to be measured by our set-up. As a result, it was necessary to study levels which could be excited from the 5d6s metastable state, which contains only a small fraction of the total ion beam. Another difficulty arose as a result of large hyperfine effects in Lu II, as discussed in section 3.3. These hyperfine structure effects gave rise to laser resonances much wider than the exciting radiation, and hence only a fraction of those ions in the metastable state could be excited. In total, we expect that only a few percent at most of the total lutetium beam was excited to the energy levels of interest.[24]

Since such a small fraction of the ion beam actually became excited to the appropriate level, it was necessary to have as high an ion beam current as possible. This, too, posed problems, as the high ion beam gave rise to a high beam background. In addition, it was very difficult to obtain a high lutetium beam current. One complication

concerned the contamination of ytterbium in the lutetium beam. This contamination was not a result of impure samples or carelessness, rather, it was a result of the need to reuse old ion source parts when making repairs or replacements. As ytterbium was studied before in the astrophysics laboratory, many of the spare parts still had traces of ytterbium on them. Ytterbium has isotopes at 174 and 176 a.m.u., while the lutetium mass peak is at 175 a.m.u. Since the lutetium required a much higher temperature than the ytterbium to vaporize and produce a beam, any ytterbium in the source completely dominated the mass profile until the vaporization temperature for lutetium was reached. The high temperature required also caused difficulty, as it was close to the maximum temperature the equipment was capable of producing. In addition, the lutetium often melted without producing a strong beam, coating everything inside the source and causing short circuits as insulating ceramics became coated with the metal. Occasionally, the lutetium evaporated all at once, producing a very strong beam current for a few seconds, but not a stable beam which could be used for the experiment. One filling of the oven typically lasted 1-2 days, with at least an hour of running the accelerator (to 'burn out' the ytterbium and allow the lutetium to be heated at a slow rate) necessary to attain an acceptable lutetium beam. A typical lutetium beam was about 0.5 μA, a much lower current than is commonly obtained for other elements.

In spite of these experimental difficulties, each level was measured a minimum of 10 times (typically around 25), and for each measurement, successive sweeps were summed to give a peak value of least 100 counts for the net signal. Since the background signal was so high compared to the decay signal, many sweeps were required to get a decay curve significantly out of the background.

The lifetimes of the measured levels of singly ionized lutetium are listed in Tables 5.2.2, 5.2.4, 5.2.6, and 5.2.6, with experimental uncertainties. Specifics of measuring each line introduce the tables of results. Previous measurements, as well as HFR calculations are given in the tables for comparison.

5.2.1 The Measurement of the Transition at 307.8 nm

The width of this line (FWHM) was expected to be approximately 0.0099 nm, as calculated in Chapter 3. As can be seen in Figure 5.1 below, the observed width of the line was approximately 0.009 nm (1 channel = 0.0005 nm).

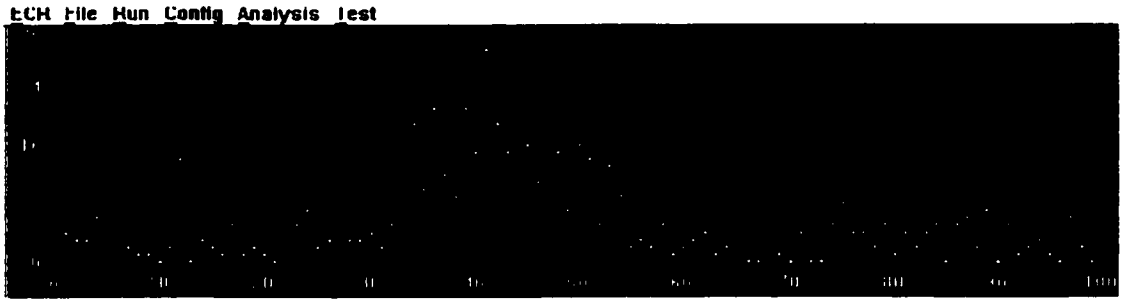


**Figure 5.1 A Typical Spectrum of the Resonance at 307.8 nm**

For this line, as well as for the other three, many measurements (typically more than twenty) were taken over a period of weeks, and sometimes even months. Various decay curves were often summed, and the summed decay curves actually fitted to obtain the lifetimes. This process was necessary because of the extremely low decay signals obtained throughout the lutetium experiment. In order to obtain sufficiently good statistics in the measurements, two or more decay curves were added together. In the Table 5.2.1 below, the decay curves used in the fitting are listed, along with the individual measurements of which they are composed.

Table 5.2.1 **Summed Decay Curves Used for Fitting Lifetime at 307.8 nm**

| Decay Curve Label | Component Curves | Fitting Result |
|---|---|---|
| 6 | 4, 5 | 4.88 ± 0.14 |
| o | 7, 8, 9 | 5.15 ± 0.11 |
| s | a, b, c, d | 4.99 ± 0.10 |
| t | e, f | 5.10 ± 0.15 |
| k | g, h, i | 5.49 ± 0.11 |
| Weighted Mean: 5.13 ± 0.09 ns<br>Mean of Individual fits: 5.04 ± 0.11 ns<br>Lifetime Result Quoted: 5.09 ± 0.18 ns | | |

The final results obtained, along with additional information about this transition, are summarized in the Table 5.2.2 below.

Table 5.2.2 **Experimental and Theoretical Lifetime Values for the Line at 307.8 nm**

| | |
|---|---|
| Energy | 44918 $cm^{-1}$ |
| Configuration | 5d6p $^3F$ |
| J-value | 3 |
| λ in air | 307.8 nm |
| Dye used | Rhodamine 590 |
| Lifetime value (This work) | 5.09 ± 0.18 ns |
| Previous Experimental lifetime [26] | 3.8 ± 0.5 ns |
| Theoretical Lifetime (HFR + CP) | 4.45 ns |

5.2.2 The Measurement of the Transition at 291.2 nm

The width of this line was expected to be approximately 0.011 nm, as calculated in Chapter 3. As can be seen in Figure 5.2 on the following page, the observed width of the line was approximately 0.012 nm (1 channel = 0.0005nm).

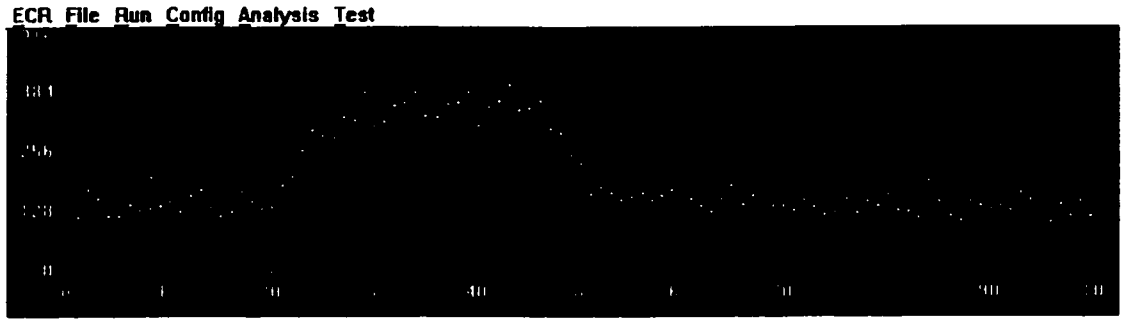


**Figure 5.2 A Typical Spectrum of the Resonance at 291.2 nm**

In order to obtain sufficiently good statistics in the measurements, two or more decay curves were added together to increase the decay signal. In the Table 5.2.3 below, the decay curves used in the fitting are listed, along with the individual measurements of which they are composed.

Table 5.2.3 **Summed Decay Curves Used for Fitting Lifetime at 291.2 nm**

| Decay Curve Label | Component Curves | Fitting Result |
|---|---|---|
| s | 2, 3, 4 | 3.82 ± 0.05 |
| t | 5, 6, 7 | 3.71 ± 0.04 |
| u | 8, 9, a, b | 4.33 ± 0.08 |
| v | c, d, e, f | 4.11 ± 0.06 |
| w | g, h, I, j | 4.33 ± 0.08 |
| n | k, l, m | 3.95 ± 0.07 |
| r | o, p, q | 3.93 ± 0.05 |
| z | x, y | 3.81 ± 0.05 |
| Weighted Mean : 3.96 ± 0.08 ns | | |
| Mean of Individual fits: 4.02 ± 0.07 ns | | |
| Lifetime Result Quoted: 3.99 ± 0.12 ns | | |

The final results obtained, along with additional information about this transition, are summarized in the Table 5.2.4 below.

Table 5.2.4 **Experimental and Theoretical Lifetime Values for the Line at 291.2 nm**

| | |
|---|---|
| Energy | 48536 $cm^{-1}$ |
| Configuration | 5d6p $^3F$ |
| J-value | 4 |
| $\lambda$ in air | 291.2 nm |
| Dye used | Rhodamine 590 |
| Lifetime value (This work) | 3.99 $\pm$ 0.12 ns |
| Previous Experimental lifetime [26] | 4.2 $\pm$ 0.4 ns |
| Theoretical Lifetime (HFR + CP) | 3.45 ns |

5.2.3 The Measurement of the Transition at 289.6 nm

The width of this line was expected to be approximately 0.011 nm, as calculated in Chapter 3. As can be seen in Figure 5.3 below, the observed width of the line was approximately 0.012 nm (1 channel = 0.001 nm).

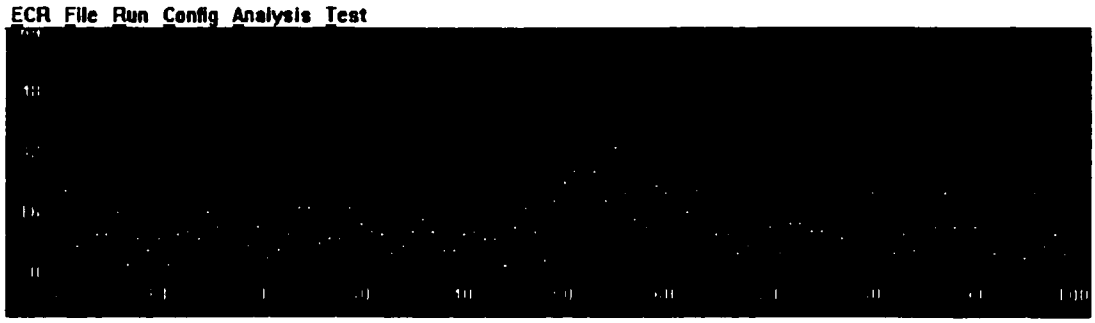


**Figure 5.3 A Typical Spectrum of the Resonance at 289.6 nm**

In order to obtain sufficiently good statistics in the measurements, two or more decay curves were added together to increase the decay signal. In the Table 5.2.5 on the next page, the decay curves used in the fitting are listed, along with the individual measurements of which they are composed.

Table 5.2.5 **Summed Decay Curves Used for Fitting Lifetime at 289.6 nm**

| Decay Curve Label | Component Curves | Fitting Result |
|---|---|---|
| s | s | 4.54 ± 0.13 |
| t | t | 4.15 ± 0.18 |
| u | u | 3.49 ± 0.28 |
| w | g, h, i, j | 3.50 ± 0.05 |
| x | k, l, m, n | 3.58 ± 0.04 |
| y | o, p, q, r, v | 3.98 ± 0.05 |
| Weighted Mean : 3.71 ± 0.16 ns<br>Mean of Individual Fits: 3.84 ± 0.11 ns<br>Lifetime Result Quoted: 3.80 ± 0.18 ns | | |

The final results obtained, along with additional information about this transition, are summarized in the Table 5.2.6 below.

Table 5.2.6 **Experimental and Theoretical Lifetime Values for the Line at 289.6 nm**

| | |
|---|---|
| Energy | 48733 $cm^{-1}$ |
| Configuration | 5d6p $^3D$ |
| J-value | 3 |
| λ in air | 289.6 nm |
| Dye used | Rhodamine 590 |
| Lifetime value (This work) | 3.80 ± 0.18 ns |
| Previous Experimental lifetime [26] | 4.0 ± 0.5 ns |
| Theoretical Lifetime (HFR + CP) | 3.06 ns |

5.2.4 The Measurement of the Transition at 279.7 nm

The width of this line was expected to be very small, as the level from which the transition was pumped was assumed to be a pure singlet. However, as can be seen in Figure 5.4 below, the observed width of the line was approximately 0.005 nm (1 channel = 0.0005 nm). This is more than twice the width expected in the absence of hyperfine

broadening. This result suggests the presence of a triplet component in the singlet D level.

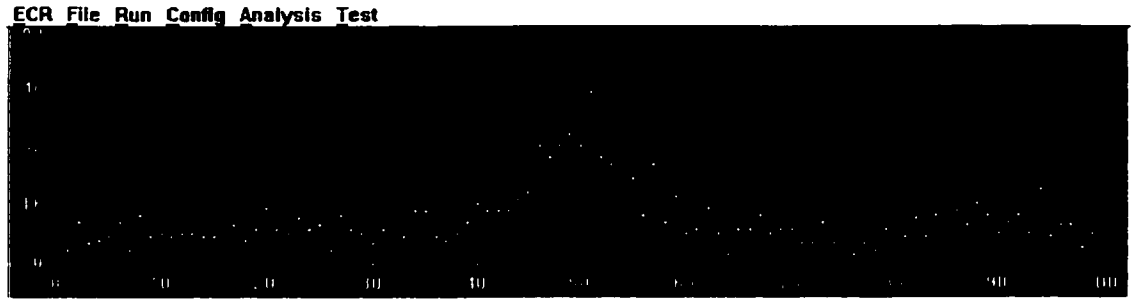


**Figure 5.4 A Typical Spectrum of the Resonance at 279.7 nm**

In order to obtain sufficiently good statistics in the measurements, two or more decay curves were added together to increase the decay signal. In the Table 5.2.7 below, the decay curves used in the fitting are listed, along with the individual measurements of which they are composed.

Table 5.2.7 **Summed Decay Curves Used for Fitting Lifetime at 279.7 nm**

| Decay Curve Label | Component Curves | Fitting Result |
|---|---|---|
| u | 2, 3, a, b | 3.80 ± 0.07 |
| v | e, f, g, h, j | 4.44 ± 0.05 |
| Weighted Mean: 4.15 ± 0.32 ns | | |
| Mean of Individual fits: 4.54 ± 0.12 ns | | |
| Lifetime Result Quoted: 4.49 ± 0.13 ns | | |

The final results obtained, along with additional information about this transition, are summarized in the Table 5.2.8 on the following page.

Table 5.2.8 **Experimental and Theoretical Lifetime Values for the Line at 279.7 nm**

| | |
|---|---|
| Energy | 53079 $cm^{-1}$ |
| Configuration | 5d6p $^1F$ |
| J-value | 3 |
| $\lambda$ in air | 279.7 nm |
| Dye used | Coumarin 540A |
| Lifetime value (This work) | $4.49 \pm 0.13$ ns |
| Previous Experimental lifetime | N/A |
| Theoretical Lifetime (HFR + CP) | 3.96 ns |

5.3 Discussion of the Lutetium Results

The HFR+CP calculations quoted in Tables 5.2.1 to 5.2.4 are in good agreement with our experimental measurements. The mean ratio of experimental lifetime to calculated lifetime is $1.17 \pm 0.05$. Table 5.3.1 on the following page shows a set of recently published [25] Lu II results, including, but not limited to, the lifetime measurements quoted in Section 5.2.

Our results also show further evidence of hyperfine structure effects in Lu II. For the 5d6s $^3D_3$ - 5d6p $^3D_3$ and 5d6s $^3D_3$ - 5d6p $^3F_4$ transitions, the laser resonances had widths of approximately 0.012 nm, which is very close to the width of 0.011 nm expected from hyperfine splitting in the 5d6s $^3D_3$ level (section 3.3). This agreement shows that the hfs contribution from the 5d6p levels is much smaller. As well, we have seen resonance widths of about 0.005 nm for the 5d6s $^1D_2$ - 5d6p $^1F_3$ transition, suggesting a non-negligible hfs width in the $^1D_2$ level. Obviously, if the level was purely a singlet, the hfs width would be zero. However, the coupling is far from perfect LS, as evidenced in the relative spacing of the 5d6s and 5d6p configurations. This is further supported by the Quinet et al calculation and by the resolved hyperfine structure observed for this line by Lawler et al.

**Table 5.3.1 Experimental and Theoretical Lifetimes for Levels in Lu II**

| Energy[a] $cm^{-1}$ | Level[a] | Experimental τ (ns) Previous | This Work | Theoretical τ (ns) Previous[e] | Recent[f] |
|---|---|---|---|---|---|
| 27264.40 | $6s6p\ ^3P_0$ | $61 \pm 5$[b] | | | 69.66 |
| 28503.16 | $6s6p\ ^3P_1$ | $37 \pm 4$[b] | | | 37.60 |
| 32453.26 | $6s6p\ ^3P_2$ | $42 \pm 6$[c] | | | 46.47 |
| 41224.96 | $5d6p\ ^3F_2$ | $3.7 \pm 0.4$[d] | | 5.18 | 5.31 |
| 44918.68 | $5d6p\ ^3F_3$ | $3.8 \pm 0.5$[d] | $5.09 \pm 0.18$ | 4.21 | 4.45 |
| 45458.56 | $5d6p\ ^1D_2$ | $2.8 \pm 0.3$[d] | | 3.92 | 3.86 |
| 45532.33 | $5d6p\ ^3D_1$ | $3.1 \pm 0.2$[b] | | 2.51 | 2.81 |
| 46904.38 | $5d6p\ ^3D_2$ | $3.8 \pm 0.5$[d] | | 3.01 | 3.05 |
| 48536.83 | $5d6p\ ^3F_4$ | $4.2 \pm 0.4$[d] | $3.96 \pm 0.16$ | 3.25 | 3.45 |
| 48733.19 | $5d6p\ ^3D_3$ | $4.0 \pm 0.5$[d] | $3.80 \pm 0.18$ | 2.91 | 3.06 |
| 50049.20 | $5d6p\ ^3P_1$ | $3.4 \pm 0.5$[d] | | 1.94 | 2.07 |
| 53079.33 | $5d6p\ ^1F_3$ | | $4.50 \pm 0.22$ | | 3.96 |

a) From Martin et al (1978) [27].
b) Li and Lundberg (1998): time-resolved-laser spectroscopy [7].
c) Den Hartog et al (1998): laser-induced fluorescence [4].
d) Andersen and Sorensen(1974) [26], Andersen et al (1975) [6]: beam-foil.
e) Bord et al (1998): HXR calculations [5].
f) HFR + CP results [25]

## 5.4 The Thulium Experiment

Sixteen levels were measured in singly-ionized thulium; fifteen of these being chosen because the theoretical and experimental lifetime levels were in poor agreement. The frequency-doubling BBO crystal was used with the excimer-pumped dye laser for those transitions below approximately 300nm. Various dyes were used to obtain the required wavelengths, as shown in Table 5.2. Typical values for the thulium beam current were around 1-3 μA.

Although far fewer problems were encountered with thulium (when compared with lutetium) in the actual running of the experiment, several tests were performed on the experimental data to check for possible systematic problems in levels with lifetimes around 20 ns or longer. One anticipated problem was misalignment of the ion beam with the direction of travel of the optical detection system. Another possibility is that the ion beam might diverge significantly enough so that some of the ions may pass outside the detection region for points far from the excitation region.

One test involved checking for systematic differences in the lifetime values for decay curves measured at different ion energies, and hence beam velocities. For levels with lifetimes of 10 ns or more, measurements were taken at 150 keV and 250 keV. The 150 keV data covered a distance approximately 25% shorter than the 250 keV data, as the 150 keV accelerating voltage produces a smaller beam velocity. This test revealed a possible systematic problem with lifetimes longer than 20 ns. For the lifetimes up to and including 20 ns, the mean lifetime at 150 keV divided by the mean value at 250 keV is $0.99 \pm 0.06$, whereas for the lifetimes longer than 20 ns, this ratio is $1.10 \pm 0.03$. In the

quoted results, for cases where the two energies gave significantly different lifetime values, only the 150 keV values were used.

The other test for systematic error involved examination of the ion beam current (I) and the beam background (B). The ion beam current (I) and beam background (B) signals were fitted to a straight-line graph using MATHCAD software. Although only one individual decay curve showed a systematic variation in ion beam current along the curve, 110 out of the 119 individual decay curves used in the analysis showed a significant variation in the beam background. These variations resulted in a change of the lifetimes calculated from the affected decay curve, ranging from 0-10%. However, this likely represents an over-correction of the possible divergence or mis-alignment effects because the laser beam has a typical height of 3mm, while the ion beam has a diameter of 5mm. Misalignment will have a greater effect on the ions excited by residual gas than those excited by the laser, as all of the beam is potentially involved in residual gas excitation, while only the portion overlapped by the laser spot will be involved in the decay signal. As a result, half of the beam-variation correction was used in compiling the list of final lifetimes from the individual data sets, with the magnitude of this "half" correction included in the calculation of the uncertainty in each individual lifetime value.

The lifetimes of the measured levels of singly ionized thulium are listed in Table 5.4.1, with experimental uncertainties. Previous measurements and theoretical calculations are also given in the table for comparison.

**Table 5.4.1 Experimental and Theoretical Lifetimes for Levels in Tm II**

| Energy[a] $cm^{-1}$ | Config.[a] | J | λair (nm) | Lifetime (ns) This Work | Prev. Exp.[b] | Theor.[c] |
|---|---|---|---|---|---|---|
| 26575 | $4f^{12}5d6s$ | 4 | 379.58[1] | 20.4 ± 0.4 | 20.2 | 21.1 |
| 26579 | $4f^{12}6s^2$ | 3 | 376.19[2] | 27.5 ± 0.4 | 27.0 | 46.7 |
| 27009 | $4f^{12}5d6s$ | 4 | 370.14[1] | 32.1 ± 1.3 | 38.2 | 28.9 |
| 27254 | $4f^{12}5d6s$ | 4 | 370.03[1] | 35.6 ± 2.1 | 38.7 | 41.0 |
| 28875 | $4f^{12}5d6s$ | 5 | 346.22[3] | 19.0 ± 0.2 | 18.5 | 14.7 |
| 29967 | $4f^{12}5d6s$ | 2 | 336.26[4] | 11.3 ± 0.2 | 10.7 | 13.1 |
| 31927 | $4f^{12}5d6s$ | 5 | 313.13[5] | 9.0 ± 0.2 | 9.1 | 13.1 |
| 38094 | $4f^{12}5d6s$ | 4 | 262.43[6] | 20.6 ± 0.3 | 20.5 | 47.0 |
| 38361 | $4f^{12}5d6s$ | 4 | 260.60[6] | 44 ± 3 | 47.3 | 24.7 |
| 38583 | $4f^{12}6d^2$ | 3 | 260.70[6] | 17.7 ± 0.3 | 17.2 | 23.7 |
| 39026 | $4f^{12}5d6s$ | 4 | 256.17[6] | > 60 [d] | 79.7 | 29.0 |
| 39162 | $4f^{12}5d6s$ | 4 | 256.83[6] | 19.3 ± 0.5 | 17.5 | 27.5 |
| 40545 | --------- | 3 | 248.01[6] | 14.2 ± 0.2 | 14.4 | 22.6 |
| 53104 | $4f^{12}5d6p$ | 6 | 246.49[6] | 4.4 ± 0.3 [e] | 4.1 | 3.1 |
| 53305 | $4f^{12}5d6p$ | 7 | 244.74[6] | 3.93 ± 0.09 | 3.7 | 2.8 |
| 53739 | $4f^{12}5d6p$ | 7 | 242.17[6] | 4.06 ± 0.06 | 4.0 | 3.2 |

1) BPBD dye 2) BPBD + BBQ 3) PTP 4) CV 670 5) Kiton Red 620 6)C-500

a) W.C. Martin et al [27]
b) Previous measurement using laser excitation of ions excited in a hollow cathode discharge by H.M. Anderson et al [8]
c) HFR calculation by P. Quinet at al [9]
d) Lifetime too long for our technique. Our value represents a lower limit only.
e) Relatively large uncertainty assigned as this result relies on only a single decay curve measurement.

5.5 Discussion of Thulium Results

Of the sixteen levels studied, one (26575 $cm^{-1}$) was studied as a test case, since there was no disagreement between previous calculation [9] and experiment [8]. Our value also agrees with both previous values, although it is closer to the experimental result. Of the remaining fifteen levels, our work confirms the previous experimental value in thirteen cases (the previous experimental values were quoted as having an overall accuracy of 5%). For the level at 39026 $cm^{-1}$, our result also supports that measured by Anderson et al. They quote a lifetime of 79.7 ns, which is well beyond the limits of our equipment. Our measurement suggests a lifetime greater than 60 ns and is therefore in disagreement with the much shorter value calculated by Quinet et al. However, for the final level, that at 27009 $cm^{-1}$, our measurement lies intermediate between the experimental value reported by Anderson et al and the theoretical value given by Quinet et al. Discussions with both of these groups, and a re-examination of our data, have failed to explain this remaining discrepancy. An independent measurement is therefore needed to establish the lifetime of this level.

Generally, it can be concluded based on our experimental results that the lifetime measurements of Anderson et al are likely accurate to within the quoted uncertainty of $\pm$ 5%, except for the level at 39007$cm^{-1}$. For that level, an independent measurement is necessary to establish the lifetime. Our results have uncertainties significantly less than $\pm$ 5%. The average uncertainty for the eleven levels for which the lifetime was near or below 20ns is 1.5%, excluding the level at 53014$cm^{-1}$, which relied only on a single decay curve. Notably, the uncertainty increases with increasing lifetime, suggesting that our experimental process may have difficulties with long lifetimes. However, after

performing the tests described in section 5.3, we are confident that our results in Table 5.2 are accurate to within their quoted uncertainties. In addition, we were able to demonstrate that our experimental setup is not subject to significant systematic difficulties for lifetimes up to 40ns. Further support for this has been given by a new measurement by Li et al of the lifetime of the level at 33654 $cm^{-1}$ in Yb II. Li et al report a value of 39 $\pm$ 3 ns [28], which is consistent with that measured in this laboratory. A recent measurement here gave a lifetime for that level of 37.7 $\pm$ 0.5 ns. However, in the light of the tests described here of the Tm II measurements for longer-lived levels, it would appear that the error estimate quoted for the Yb II result may perhaps be somewhat optimistic. (That result did not include the specific tests made in the Tm II measurements.)

# CHAPTER VI: EPILOGUE

## 6.1 Epilogue

There continues to be a need for lifetime measurements for rare earth elements. Although we at the University of Alberta have been successful in studying four of the levels in singly ionized lutetium, the inherent experimental difficulties and the time-consuming nature of our fast beam-laser technique prevented the examination of many Lu II levels. In spite of the challenge involved in Lu II lifetime measurements, the recent astrophysical interest in Lu II due to its discovery in certain chemically peculiar and rapidly oscillating Ap stars makes it a worthwhile project. As ytterbium contamination was a common problem, a possible improvement would be to use only new parts in the ion source. Use of those parts as replacement components could then be confined to lutetium studies. Production of a stronger (at least a few μA) ion beam might also make the experiment less problematic, as our low beam led to a poor signal-to-noise ratio, necessitating many more data sweeps than are normally required to obtain a good data curve, and hence, taking much more time.

Overall, I feel that our lutetium project was successful. We obtained improved experimental radiative lifetime values for four levels of Lu II, and saw further evidence of the previously documented hyperfine structure of Lu II [29]. The Lu II results have been presented at both the ASOS-6 meeting in Victoria, BC in August 1998, and the CAP meeting in Fredericton, NB in 1999. In addition, these results will shortly appear in the prestigious journal *Monthly Notices of the Royal Astronomical Society*, as part of a joint project with the Liege and Madison groups. In light of this success, I believe that it would be worthwhile for another group to pursue study of other lutetium energy levels

using modern technology (perhaps faster electronics to speed up data collection) to overcome some of the experimental difficulties which perhaps are the reason for the scarcity of experimental lutetium data in the literature.

There is also interest in the thulium spectrum in the study of stellar abundances. Our measurements of levels in the singly ionized thulium spectrum were also a success. Our results confirmed the previous experimental results concerning thirteen of the fifteen levels in serious disagreement with calculation. The Tm II results have been accepted for publication in *Physics Review A*. As our work did not confirm the theoretical calculations, our results may be seen as a starting point in revising the theoretical models used in the calculation. Unfortunately, the time-consuming nature of our technique prevented study of all the published lifetime values for Tm II. Although our success in confirming the experimental results suggests the published values are correct, more work should be done to check this and also to improve the accuracy for the remaining levels beyond the 5% quoted by Anderson et al. Furthermore, there were many levels having lifetimes too long for our equipment to measure. These should be studied by another technique, which is capable of measuring lifetimes in the 40 ns to 200 ns range.

Another important result from our project was that we were able to establish the validity of our technique for lifetimes in the range 20 ns to 40 ns. The tests we performed on the thulium data concerning lifetime fluctuations with different acceleration voltages showed that, although there was a possible problem, it should not affect our results significantly if sufficient care is taken in the measurement. We were able to reconfirm the validity of our method for lifetimes less than 20 ns, and to show that any problems our technique may have for lifetimes greater that 20 ns cause greater experimental error

but still give valid results. However, these results do suggest that in some of the previous measurements in this laboratory the experimental uncertainties may have been somewhat under-estimated for lifetimes having values close to 40 ns.

Overall, I feel the beam laser technique used in our astrophysics lab is a good one. It allowed good time resolution, allowing study of levels with short lifetimes of the order of a few nanoseconds. As well, our success in obtaining radiative lifetimes for lutetium may lead other groups to add to the experimental data bank of lutetium, and perhaps to find new methods which would overcome some of the difficulties we encountered.

## References


[1] Jaschek M. and Brandi E., Astron. Astrophys., 20, 233, (1972).

[2] Jaschek C. and Jaschek M., The Behavior of Chemical Elements in Stars, Cambridge University Press (1995).

[3] Grevesse N. and Blanquet G., Solar Phys., 8, 5, (1969).

[4] Den Hartog E.A., Curry J.J., Wickliffe M.E., Lawler J.E., Solar Physics, 178, 239, (1998).

[5] Bord D.J., Cowley C.R. and Mirijanian D., Solar Phys. (submitted 1999).

[6] Andersen T., Poulsen O., Ramanujam P.S., Petrakiev Petkov A., Solar Phys., 44, 257, (1975).

[7] Li Z. and Lundberg H., Communication presented at the ASOS-6 meeting in Victoria, Canada, (1998).

[8] Anderson H.M., Den Hartog E.A., and Lawler, J.E., J. Opt. Soc. Am. B, 13, 2382, (1996).

[9] Quinet P., Palmeri P., and Biemont E., J. Quant. Rad. Spectr. Trans., (in press 1999).

[10] Schultz-Johanning M., Schnabel R., and Kock M., Eur. Phys. J. D, 5, 341, (1999).

[11] Lowe R.M., Hannaford P., and Martennson Pendrill A.-M., Z. Phys. D, 283, (1993).

[12] Unsold A., The New Cosmos, Springer-Verlag, New York (1969).

[13] Cowley C.R., The Theory of Stellar Spectra, Gordon and Breach, New York (1970).

[14] Phys 462 lecture notes, 1997.

[15] Migdalek J., Baylis W.E., J. Phys. B, 11, L497, (1978).

[16] Cowan R.D., The Theory of Atomic Structure and Spectra, University of California Press, Berkeley, (1981).

[17] Weast R.C., ed., Handbook of Chemistry and Physics, The Chemical Rubber Co., Cleveland, Ohio, (1970).

[18] Steudel A., Zeit f Phys., 152, 599, (1958).

[19] Bashkin S., ed., J. Opt. Soc. Am., 61, 1686, (1971).

[20] Pinnington E.H., Berends R.W., and Lumsden M., J. Phys. B At. Mol. Opt. Phys., 28, 2095, (1995).

[21] Corney A., Atomic and Laser Spectroscopy, Clarendon Press, Oxford, (1983).

[22] Gosselin R.N., Ph.D Thesis, Univ. of Alberta, Edmonton (1988).

[23] Horlick G., Applied Spectroscopy, 30, 113 (1976).

[24] Gosselin R.N., Pinnington E.H., and Ansbacher W., Physical Review A, 38, 4887 (1988).

[25] Quinet P., Palmeri P., Biemont E., McCurdy M.M., Rieger G., Pinnington E.H., Lawler J.E., and Wickliffe M.E., MNRAS (in press 1999).

[26] Andersen T., Sorensen G., Solar Phys., 38, 343 (1974).

[27] Martin W.C., Zalubas R., Hagan L., Atomic Energy Levels – The Rare Earth Elements, Nat'l Stand. Ref. Data Ser. (NBS), 60 (1978).

[28] Li Z.S., Svanburg S., Quinet P., Tordoir X., and Biemont E., J. Phys. B. At. Mol. Opt. Phys., 32, 1731 (1999).

[29] Pinnington E.H., Can. J. Phys., 41, 1294 (1963).